A single-cell atlas of *E. faecalis* wound infection reveals novel bacterial-host immunomodulatory mechanisms

Cenk CELIK[1,5], Stella Yue Ting LEE[1], Frederick Reinhart TANOTO[2], Mark VELEBA[2], Kimberly A. KLINE[1,2,3], Guillaume THIBAULT[1,4]

[1]School of Biological Sciences and [2]Singapore Centre for Environmental Life Science Engineering, Nanyang Technological University, Singapore

[3]Department of Microbiology and Molecular Medicine, Faculty of Medicine, University of Geneva, Switzerland

[4]Mechanobiology Institute, National University of Singapore, Singapore

[5]Present address: Department of Genetics, Evolution and Environment, Genetics Institute, University College London, London, UK

Correspondence to:

Kimberly Kline, Tel: +41 (0)22 379 56 02; email: Kimberly.Kline@unige.ch

Guillaume Thibault, Tel: +65 6592 1787; email: thibault@ntu.edu.sg

Running title: Infected wound single-cell atlas

ABSTRACT

Wound infections are highly prevalent, and can lead to delayed or failed healing, causing significant morbidity and adverse economic impacts. These infections occur in various contexts, including diabetic foot ulcers, burns, and surgical sites. *Enterococcus faecalis* is often found in persistent non-healing wounds, but its contribution to chronic wounds remains understudied. To address this, we employed single-cell RNA sequencing (scRNA-seq) on infected wounds in comparison to uninfected wounds in a mouse model. Examining over 23,000 cells, we created a comprehensive single-cell atlas that captures the cellular and transcriptomic landscape of these wounds. Our analysis revealed unique transcriptional and metabolic alterations in infected wounds, elucidating the distinct molecular changes associated with bacterial infection compared to the normal wound healing process. We identified dysregulated keratinocyte and fibroblast transcriptomes in response to infection, jointly contributing to an anti-inflammatory environment. Notably, *E. faecalis* infection prompted a premature, incomplete epithelial-to-mesenchymal transition in keratinocytes. Additionally, *E. faecalis* infection modulated M2-like macrophage polarization by inhibiting pro-inflammatory resolution *in vitro*, *in vivo,* and in our scRNA-seq atlas. Furthermore, we discovered macrophage crosstalk with neutrophils, which regulates chemokine signaling pathways, while promoting anti-inflammatory interactions with endothelial cells. Overall, our findings offer new insights into the immunosuppressive role of *E. faecalis* in wound infections.

AUTHOR SUMMARY

Wound infections, including diabetic foot ulcers, burns, or surgical sites, often lead to prolonged healing and significant health and economic burdens. Among the bacteria implicated in these persistent wounds, *Enterococcus faecalis* remains a relatively enigmatic player. To unravel its role in non-healing wounds, we used single-cell RNA sequencing in a mouse model, scrutinizing over 23,000 cells to construct a comprehensive single-cell map of infected wounds compared to uninfected wounds. Our investigation revealed distinct genetic and metabolic alterations in infected wounds, in which infection resulted in a perturbed inflammatory environment delayed wound healing signatures. Specifically, *E. faecalis* infection induces a premature and incomplete transition in keratinocytes, impeding their healing function. Furthermore, infection influences the behavior of immune cells like macrophages, affecting the body's response to the infection. These findings not only shed light on *E. faecalis*'s role in delayed wound healing but also offer potential avenues for future treatments, providing valuable insights into the challenging realm of wound infections.

INTRODUCTION

Infections pose a challenge to the wound healing process, affecting both the skin's protective barrier and the efficient repair mechanisms required for tissue integrity. The skin, the largest and most intricate defense system in mammals, exhibits unique cellular heterogeneity and complexity that maintain tissue homeostasis. Within the skin, undifferentiated resident cells are the main modulators of tissue maintenance, albeit terminal differentiation dynamics adapt to the regenerative requirements of the tissue. Several comprehensive studies conducted in mice and humans have highlighted the complexity of the skin[1-7]. However, these studies have primarily focused on cellular heterogeneity and the transcriptome of intact skin or uninfected wounds, offering limited insights into the dynamics of wound healing following infection.

Efficient healing during wound infections involves a sequence of events occurring in three distinct but interconnected stages: inflammation, proliferation, and remodeling[8-11]. These events involve a series of inter- and intracellular molecular interactions mediated by soluble ligands and the innate immune system[12, 13]. The inflammatory phase initiates migration of leukocytes into the wound site to help clear cell debris and establish tissue protection through local inflammation. Initially, neutrophils, responding to pro-inflammatory cytokines like IL-1β, TNF-α, and IFN-γ, extravasate through the endothelium to the site of injury. Subsequently, the proliferative stage aims to reduce wound size through contraction and re-establishment of the epithelial barrier. This stage is facilitated by activated keratinocytes modulated by inflammatory responses, cytokines, and growth factors. In the final stage, tissue remodeling restores the mechanical properties of intact skin through ECM reorganization, degradation, and synthesis[13]. Dysregulation of this intricate mechanism can lead to pathological outcomes characterized by persistent inflammation and excessive ECM production[14].

Enterococcus faecalis (*E. faecalis*) is a commensal bacterium in the human gut, and also an opportunistic pathogen responsible for various infections, including surgical site infections and diabetic ulcers[15]. Bacterial wound infections in general, including those associated with *E. faecalis,* are biofilm-associated, resulting in an antibiotic-tolerant population that may lead to persistent infections[16]. Additionally, *E. faecalis* has mechanisms to evade and suppress immune clearance by, for example, suppressing the pro-inflammatory M1-like phenotype in macrophage and preventing neutrophil

extracellular trap (NET) formation[15, 17, 18] *E. faecalis* can also persist[19-27] and replicate[28, 29] within epithelial cells and macrophages, further complicating treatment. The combination of biofilm formation and immune evasion makes Enterococcal wound infections a significant clinical challenge.

In a murine full-thickness excisional wound model, our prior investigations revealed a bifurcated trajectory characterizing *E. faecalis* wound infections[30]. Initially, bacterial colony-forming units (CFU) increase in number in the acute replication phase, with a concomitant pro-inflammatory response characterized by pro-inflammatory cytokine and chemokine production coupled with neutrophil infiltration. In the subsequent persistence stage, *E. faecalis* CFU undergo gradual reduction and stabilization at approximately 10^5 CFU within wounds by 2-3-day post-infection (dpi), coinciding with delayed wound healing. Within this framework, we have identified specific bacterial determinants that contribute to each phase of *E. faecalis* infection. For example, *de novo* purine biosynthesis emerges as a pivotal factor in enhancing bacterial fitness during the acute replication phase[31]. In the persistent phase at 3 dpi, the galactose and mannose uptake systems, in conjunction with the *mprF* gene product, are associated with nutrient acquisition and resistance to antimicrobial peptides and neutrophil-mediated killing, respectively[30, 32-35]. Nonetheless, the intricate interplay between these *E. faecalis* persistence-associated virulence factors, their immunomodulatory evasion strategies, and precise implications in the context of delayed wound healing remains to be investigated.

To address this, we generated a comprehensive single-cell atlas of the host response to persistent *E. faecalis* wound infection. We observed that *E. faecalis* induces immunosuppression in keratinocytes and fibroblasts, delaying the immune response. Notably, *E. faecalis* infection prompted a premature, partial epithelial-to-mesenchymal transition (EMT) in keratinocytes. Moreover, macrophages in infected wounds displayed M2-like polarization. Our findings also indicate that the interactions between macrophages and endothelial cells contribute to the anti-inflammatory niche during infection. Furthermore, *E.* faecalis-infected macrophages drive pathogenic vascularization signatures in endothelial cells, resembling the tumor microenvironment in cancer. We also noted *E. faecalis* infected-associated macrophage crosstalk with neutrophils, regulating chemokine signaling pathways and promoting anti-inflammatory interactions with endothelial cells. These insights from our scRNA-seq

atlas provide a foundation for future studies aimed at investigating bacterial factors contributing to wound pathogenesis and understanding the underlying mechanisms associated with delayed healing.

RESULTS

E. faecalis infection inhibits wound healing signatures

In the wound environment, various cell types, including myeloid cells, fibroblasts, and endothelial cells, play critical roles in the initial and later stages of wound healing by releasing platelet-derived growth factor (PDGF). Additionally, macrophages secrete epidermal growth factor (EGF) in injured skin, which operates through the epidermal growth factor receptor (EGFR) to promote keratinocyte proliferation, migration, and re-epithelialization. To understand the impact of *E. faecalis* infection on wound healing, we infected excisional dorsal wounds on C57BL/6J male mice and measured gene expression levels of wound healing markers in bulk tissue at 4 dpi at the onset of persistent infection. We then compared the expression profiles with those of (i) wounded but uninfected or (ii) unwounded and uninfected controls, ensuring that the uninfected and infected mice were of comparable weight (**Figures 1A**, **S1A**, and **S1B**). We observed lower expression of platelet-derived growth factor subunit A (*Pdgfa*) in *E. faecalis*-infected wounds than in unwounded skin, while uninfected wounds remained unchanged. Similarly, the expression of *Egf* was lower in uninfected wounds than in healthy skin, while reaching the lowest levels in *E. faecalis*-infected wounds. The reduced *Egf* expression in uninfected wounds at 4 days post-wounding is expected, as EGF primarily influences skin cell growth, proliferation, and differentiation during the later stages of wound healing, typically around 10 days post-injury[36]. By contrast, expression of transforming growth factor beta 1 (*Tgfb1*) was aggravated by wounding alone. TGF-β1 plays a dual role in wound healing depending on the microenvironment. During tissue maintenance, TGF-β1 acts as a growth inhibitor, and its absence in the epidermis leads to keratinocyte hyperproliferation[37]. Elevated TGF-β1 levels have also been observed in the epidermis of chronic wounds in both humans and mouse models[38, 39]. In addition, we observed a slightly higher expression of fibroblast growth factor 1 (*Fgf1*) in uninfected wounds, although the differences were comparable (**Figure S1A**). Overall, the lower expression of *Pdgfa* and higher expression of *Tgfb1* might serve as indicators of persistent *E. faecalis*-infected wounds in the skin.

Single-cell transcriptomes of full-thickness skin wounds diverge during healing and infection

To understand the cellular heterogeneity in the wound environment following *E. faecalis* infection, we dissociated cells from full-thickness wounds, including minimal adjacent healthy skin. We generated single-cell transcriptome libraries using the droplet-based 10X Genomics Chromium microfluidic partitioning system (**Figure 1B** and **Table S1**). By integrating the transcriptomes of approximately 23,000 cells, we employed the unbiased graph-based Louvain algorithm to identify clusters[40]. Our analysis revealed 24 clusters, irrespective of infection (**Figure S1C**). These clusters included epithelial, immune, fibroblast, endothelial, vascular, and neural cell types (**Figures 1C**, **1D**, **S1D**, **S1E**, and **Tables S2-S4**). Within the epithelial class, we identified basal (BAS1-3) and suprabasal (SUP1-4) keratinocytes, hair follicles (HFSUP1-2), outer bulge (OB), and sebaceous gland (SG) cells (**Figure 1E**). The immune class included macrophages (MC1-2), neutrophils (NEUT1-2), memory T cells (TC), and a mixed population (DC/LC) of dendritic cells (DCs) and Langerhans cells (LC). Notably, cells from infected wounds (~13,000 cells) demonstrated distinct clustering patterns compared to cells from uninfected wounds (~9,500 cells) (**Figure S1F** and **Table S1**).

We proceeded to analyze upregulated gene signatures for each Louvain cluster (**Figure 1F** and **Table S2**) and compared them to the cell-type signature database[41] (PanglaoDB) to identify characteristic gene expression patterns (**Figure 1G**). Additionally, we identified highly expressed genes in uninfected and infected wounds (**Tables S3** and **S4**) and performed co-expression network analysis (WGCNA) to uncover the core genes associated with cell types (**Figure 1H**).

We also delineated macrophage populations (**Figure S1G-I**), identifying an M2-like polarization (**Figure 1F**, MC1) marked by higher expression of *Arg1*, *Egr2*, *Fn1*, and *Fpr2* (**Figure S1G**), and a tissue-resident macrophage (TRM) population (**Figure 1F**, MC2) expressing *Ccr5*, *Cd68*, *Fcgr1*, *Mrc1* (*Cd206*), *Ms4a4c*, and *Pparg* (**Figure S1H**). Both macrophage populations exhibited limited expression of *Grp18* and *Nos2* (*iNos*), which are typically associated with M1-like polarization (**Figure S1I**). Together, our analysis outlined the differences observed in uninfected and infected wound healing across epithelial, fibroblast, and immune cell populations.

***E. faecalis* elicit immunosuppressive interactions with keratinocytes**

Keratinocytes, the predominant cell population in the skin, include undifferentiated (basal) and differentiated (suprabasal, hair follicle, outer bulge, and sebaceous gland) cells within the EPI cell class in both wound types (**Figure 1C**). Further analysis of the EPI class revealed 19 clusters (**Figure 2A** and **Table S5**), with the emergence of infection-specific clusters (**Figure 2B**, clusters 0 and 6, and **S2A**). We identified three major keratinocyte populations: (i) *Krt5*-expressing (*Krt5*^{hi}) basal keratinocytes, (ii) *Krt10*-enriched (*Krt10*^{hi}) post-mitotic keratinocytes, and (iii) *Krt5*^{hi}*Krt10*^{hi} co-expressing populations (**Figure 2C**). The co-expression of *Krt5* and *Krt10* was unique to infection-specific clusters (**Figure 2A**, clusters 0 and 6). We also observed distinct populations, including hair follicle stem cells (*Lrg5*^{hi}; cluster 10), differentiating basal cells (*Ivl*^{hi}; clusters 7 and 8), terminally differentiated keratinocytes (*Lor*^{hi}; clusters 2, 8, 16, 17), and bulge stem cells (*Krt15*^{hi}; clusters 2, 9, 10, 17, 18) (**Figure 2D**), reflecting the skin's complexity.

The two largest infection-specific clusters exhibited distinct gene expression patterns, with cluster 0 and cluster 6, enriched in *Zeb2* and *Gjb6* expression, respectively (**Figure 2A**). These clusters represent migratory stem-like and partial EMT keratinocyte populations (**Figure 2E**). Additionally, *Zeb2*^{hi} keratinocytes co-expressing *Cxcl2*, *Il1b,* and *Wfdc17*, indicate an immunosuppressive environment during *E. faecalis* infection[42, 43]. Gene Ontology analysis revealed that the *Zeb2*^{hi} and *Gjb6*^{hi} clusters exhibited signatures related to ECM remodeling, chemokine signaling, migratory pathways, and inflammatory response (**Figures 2F**, **2G**, and **Table S5**). Collectively, these findings suggest an early migratory role of keratinocytes induced by *E. faecalis* infection.

During cutaneous wound healing, keratinocytes enter a mesenchymal-like state, migrating to and proliferating within the wound site. We observed two infection-specific keratinocyte populations enriched in *Zeb2* and *Gjb6* expression, respectively, as early as four days post-wounding. To determine the nature of these populations, we performed RNA velocity analysis, a method that predicts the future state of individual cells based on the patterns of temporal gene expression [44]. RNA velocity analysis predicted a lineage relationship between *Zeb2*^{hi} and *Gjb6*^{hi} keratinocytes (**Figures 2H**, **2I**, and **Table S5**). The top lineage-driver genes[45], including *Rgs1*, *H2-Aa*, *Ms4a6c*, *Cd74*, *H2-Eb1* and *H2-Ab1*, were predominantly expressed in the infection-specific cluster 0 (**Figures 2J** and **S2B**). These genes

are associated with the major histocompatibility complex (MHC), suggesting an antigen-presenting keratinocyte population. Meanwhile, *Gjb6*^{hi} keratinocytes demonstrated reduced expression of putative genes such as *Pof1b*, *Krt77*, *Dnase1l3,* and *Krtdap* as well as increased *Clic4* expression (**Figure S2C**), suggesting that *E. faecalis* infection perturbs normal healing. Additionally, temporal expression analysis of high-likelihood genes revealed three distinct transcriptional states (**Figure 2K**): (1) an early state characterized by undifferentiated (basal) keratinocyte markers, (2) an intermediate state defined by the selection and upkeep of intraepithelial T cell protein family, and (3) a late state characterized by cell adhesion signatures. These findings provide insights into the cellular dynamics and developmental abnormalities, such as partial EMT induced by *E. faecalis* infection during wound healing.

Understanding cell-cell crosstalk through ligand-receptor interactions allows predicting ligand-target links between interacting cells by combining their expression data with signaling and gene regulatory network databases. Given our observation that infection-specific keratinocyte populations (**Figure S2**) were involved in ECM remodeling and immune response (**Figures 2F** and **2G**), we hypothesized that these cells might participate in the SPP1 signaling pathway. SPP1 (secreted phosphoprotein 1 or osteopontin) is a chemokine-like protein secreted by immune cells, osteoblasts, osteocytes, and epithelial cells to facilitate anti-apoptotic immune responses[46, 47]. To decipher ligand-receptor interactions in uninfected and infected skin wounds, we performed cell-cell interaction analysis[48]. We found 34 predicted interactions in uninfected keratinocytes and 61 in keratinocytes from *E. faecalis*-infected wounds out of a total of 923 and 991 interactions, respectively, in our single-cell atlas (**Figures S1A**, **S1B**, and **Table S6**). Importantly, we detected outgoing signals from keratinocytes to other cells associated with EGF and SPP1 signaling pathways. Ligand:receptor pairs in the infected niche (**Figure S2D**) included Hbegf:Egfr for the EGF pathway and Spp1:Cd44, Spp1:(Itga5+Itgb1), Spp1:(Itga9+Itgb1), and Spp1:(Itgav+Itgb3) for the SPP1 pathway (**Figures 2L**, **S2D**, and **S2E**), that are known to induce immunosuppression[49, 50]. Remarkably, we observed the enrichment of keratinocyte-endothelial cell ligand:receptor pairs (**Figure S3** and **Table S6**). By contrast, keratinocytes from uninfected wounds only showed macrophage migration inhibitory factor (MIF) ligand interactions with its receptors Cd44, Cd74, and Cxcr4 in immune cells (DC/LC and TRM) (**Figure S2G**), suggesting that these keratinocytes promote cell proliferation, wound healing, and survival[51, 52]. Furthermore, the RNA velocity of keratinocytes from uninfected wounds revealed a terminal hair follicle (*Lrg5*^{hi}) and

a proliferating keratinocyte (*Mki67*^{hi}) population originating from basal keratinocytes (**Figure 2H**), underlining normal wound healing. Overall, *E. faecalis* infection altered the transcriptome of keratinocytes towards a partial EMT at an early stage, whereas uninfected keratinocytes showed differentiating and terminally differentiated keratinocyte populations (**Figure 2M**). Our data show that epidermal cells undergo migratory and inflammatory gene regulation during normal wound healing[53, 54], whereas *E. faecalis* induces anti-inflammatory transcriptional modulation that may promote chronicity in bacteria-infected skin wounds. These findings demonstrate that keratinocytes exist in a low inflammation profile under homeostasis, which is exacerbated upon *E. faecalis* infection.

E. faecalis delays immune response in fibroblasts

Fibroblasts are the fundamental connective tissue cells involved in skin homeostasis and healing. Upon injury, they primarily (1) migrate into the wound site, (2) produce ECM by secreting growth factors, and (3) regulate the inflammatory response. Despite their high heterogeneity, fibroblast subpopulations have distinct roles in wound healing. In response to injury, fibroblasts produce increased amounts of ECM by inhibiting the metalloproteinase (MMP) family through the tissue inhibitor of metalloproteinases 1 (TIMP1). Notably, Guerrero-Juarez *et al.* (2019) reported a rare fibroblast population expressing myeloid lineage cell markers during normal (uninfected) wound healing[48]. Our bioinformatic analysis identified fibroblast populations within wounds that differed significantly between infected and uninfected conditions (**Figure S1F**). Further analysis of the fibroblast mega class revealed 12 distinct clusters, with clusters 0 and 2 specific to infection while retaining their fibroblastic identity (**Figures 3A**, **3B**, and **Table S7**). The infection-associated fibroblasts express a range of markers, including those linked to extracellular matrix deposition such as *Col1a1*, *Col1a2*, *Col6a2*, vimentin (*Vim*), fibronectin, elastin (*Eln*), asporin (*Aspn*), platelet-derived growth factor receptor-beta (*Pdgfrb*), and fibroblast activator protein-α (*Fap*). These findings suggest a premature extracellular matrix deposition triggered by *E. faecalis*, which typically occurs in later stages of wound healing processes[55-57] (**Figures 3C**, **3D**, **S4A**, and **S4B**).

The unique fibroblast clusters 0 and 2 associated with *E. faecalis* infection (**Figure 3E**) exhibited enrichment of myeloid-specific markers (*Hbb-bs*, *Lyz2*) and profibrotic gene signatures (*Inhba*, *Saa3*, *Timp1*) (**Table S6**). Additionally, *Lyz2*^{hi} fibroblasts co-expressing *Tagln*, *Acta2*, and *Col12a1* suggested

their origin as contractile myofibroblasts[48]. Gene Ontology analysis indicated that *Lyz2*^{hi} fibroblasts were involved in immune response (**Figure 3F**), while *Timp1*^{hi} fibroblasts were associated with tissue repair processes (**Figure 3G**). These findings collectively reveal an intricate cellular landscape within infected wounds, highlighting the detrimental functional contributions of various fibroblast subpopulations in response to *E. faecalis* infection.

To validate the distinct fibroblast cell states and their differentiation potential, we performed RNA velocity analysis (**Figures 3H** and **3I**), which revealed two terminal fibroblast populations: (1) a *Cilp*^{hi} fibrotic cluster 4 and (2) an *Mkx*^{hi} reparative cluster 5, originating from clusters 0 and 2 (**Figure 3I** and **Table S7**), indicating the mesenchymal characteristics of infection-specific fibroblasts. Lineage driver gene analysis supported these findings, with the expression of genes such as *Csgalnact1*, *Atrnl1*, *Slit3*, *Rbms3*, and *Magi2*, which are known to induce fibrotic tissue formation under pathological conditions[58, 59] (**Figures 3J** and **S4C**). Similarly, the activation of genes such as *Serping1*, *Sparc*, *Pcsk5*, *Fgf7*, and *Cyp7b1* (**Figure S4D**) indicated the temporal activation of cell migration and immune suppression during infection. CellRank analysis revealed two states: an initial prolonged state and a short terminal state (**Figure 3K**). The early transcriptional states were associated with apoptosis inhibition, cell adhesion, and immune evasion genes, including serine protease inhibitors (*Serpine1* and *Serping1*), *Prrx1*, *Ncam1*, and *Chl1*, suggesting immune response suppression. By contrast, the terminal state showed the emergence of migratory (*Cd74*, *Ifi202b*) and inflammatory (*Acod1*, *Cxcl2*, *F13a1*, and *S100a9*) genes, indicating a delayed immune response to *E. faecalis* infection. Overall, these findings indicate that uninfected fibroblasts contribute to healthy wound healing with proliferative and elastin-rich fibroblast populations. By contrast, *E. faecalis*-infected fibroblasts exhibit a pathological repair profile, characterized by the presence of *Timp1*^{hi} and *Lyz2*^{hi} fibroblasts (**Figure 3L**).

To understand the role of fibroblast subpopulations in healing, we explored cell-cell interactions in fibroblasts in infected wound (**Figure S4E**). In *E. faecalis*-infected wounds, we observed interactions involving Spp1 ligand with cell adhesion receptor Cd44 and integrins (Itgav+Itgb1, Itgav+Itgb3, Itgav+Itgb5, Itga4+Itgb1, Itga5+Itgb1, Itga9+Itgb1), and EGF signaling pairing Ereg:Egfr (**Figures S4F** and **S4G**). These interactions were particularly strong between macrophages (ligands) and endothelial cells (receptors) (**Figure S2C**), suggesting their involvement in the infected wound microenvironment.

By contrast, uninfected wounds showed a normal wound healing profile with reparative VEGF and TGF-β signaling pathways (**Figures S4H** and **S4I**). Furthermore, RNA velocity analysis of fibroblasts from uninfected wounds revealed two terminal fibroblast populations originating from *Fbn1*^{hi} fibroblasts: elastin-rich (*Eln*^{hi}) fibroblasts and keratinocyte-like (*Krt1*^{hi}/*Krt10*^{hi}) fibroblasts (**Figure 3H**). Collectively, our findings revealed the unique roles of fibroblasts upon *E. faecalis* infection and reaffirmed the known functions of fibroblasts during uninfected wound healing, consistent with the outcomes of predicted ligand-receptor interactions (**Figure 3F**).

E. faecalis promotes macrophage polarization towards an anti-inflammatory phenotype

Immune cells play a crucial role in wound healing by eliminating pathogens, promoting keratinocyte and fibroblast activity, and resolving inflammation and tissue repair[53, 54, 60]. Our data reveal unique clusters enriched within keratinocytes and fibroblasts in *E. faecalis*-infected wounds, suggesting an immunosuppressive transcriptional program in these cell populations (**Figures S2A** and **S4B**). Given the ability of *E. faecalis* to actively suppress macrophage activation *in vitro*[17], we investigated if *E. faecalis* contributes to anti-inflammatory macrophage polarization and immune suppression *in vivo*. Analysis of the myeloid cells identified two infection-specific macrophage clusters (clusters 2 and 5) among 12 clusters (**Figures 4A**, **4B**, and **Table S8**). To validate infection-specific macrophage polarization, we performed qPCR on bulk tissue isolated from uninfected and infected wounds at 4 dpi. Infected wounds showed downregulation of *Mrc1* and upregulation of both *Arg1* and *Nos2* compared to uninfected wounds or unwounded bulk skin tissue (**Figure 4D**), which was further corroborated by examining gene expression in bone marrow-derived macrophages (BMDM) following *E. faecalis* infection *in vitro* (**Figure 4E**). The co-expression of both M1-like and M2-like macrophage markers during infection has been previously reported for *M. tuberculosis*[61], *T. cruzi*[62], and *G. lamblia* infections[63], as an indicator of an immunosuppressive phenotype that promotes an anti-inflammatory environment during prolonged infection. In myeloid clusters of our scRNA-seq atlas, tissue-resident macrophages (*Mrc1*) were predominant in uninfected wounds, while M2-like macrophages (*Arg1*) were abundant in macrophages from *E. faecalis*-infected wounds (**Figures 4F** and **4G**), supporting the hypothesis of an anti-inflammatory wound environment during *E. faecalis* infection. Additionally, our analysis allowed the segregation of dendritic cells and Langerhans cells (cluster 10, *Cd207* and *Itgax*)

from macrophage populations, characterized by the co-expression of langerin (*Cd207*) and integrin alpha X (*Itgax*/*Cd11c*) in cluster 10 (**Figure 4G**), confirming the validity of our cell annotation.

Next, we focused on the functions of infection-specific macrophage clusters 2 and 5 (**Figures 4B** and **S5B**) to identify their potential roles in wound infection. Gene Ontology analysis revealed that these macrophages were involved in the immune response, ECM production, and protein translation (**Figures S5C** and **S5D**). To better understand the evolution of infection-specific macrophages, we computed the RNA velocity to explore potential lineage relationships (**Figures 4H** and **4I**). RNA velocity identified cluster 2 macrophages as the terminal population in the infected dataset (**Figure 4I**), whereas uninfected terminal macrophage populations were found as clusters 1 and 4 (**Figure 4H**). As expected, cluster 5 did not exhibit velocity vectors since these cells were highly segregated from the main myeloid clusters and differed vastly in their gene expression (**Table S8**). While both terminal macrophage populations in both uninfected and infection conditions co-host anti-inflammatory macrophage signatures, their transcriptional program and functions vary in the presence of *E. faecalis* infection.

To further characterize clusters 2 and 5, we explored differentially expressed genes in infected cells. We identified the inflammation-related genes *Fth1*, *Slpi*, *Il1b*, *AA467197* (*Nmes1*/miR-147), *Ptges,* and *Cxcl3* (**Figures 4J** and **S5E**), suggesting that these cells may play a role in tissue remodeling[64, 65]. Similarly, the expression of the infected-specific top likelihood genes *Cxcl2*, *Cd36,* and *Pdpn* was associated with the presence of efferocytic M2-like macrophages (**Figure S5F**, green clusters). The distant *Sparc*^{hi} macrophage cluster 5 exhibited C-C chemokine receptor type 7 (*Ccr7*) exhaustion (**Figure S5F**, red clusters), indicating that these cells might be of M1-like origin[66].

Next, to validate whether the terminal macrophage populations corresponding to clusters 2 and 5 were tissue-resident or M2-like macrophages, we computed the driver genes of macrophage sub-clusters over latent time. The top 50 likelihood gene heat map identified two major states in the macrophages (**Figure 4K**). The early state cells were enriched in antigen-presenting/processing MHC class II gene expression such as *H2-Ab1*, *H2-Eb1, H2-Eb2,* G-protein-coupled receptors (*Gpr137b*, *Grp171,* and *Gpr183*), and mannose receptor c-type 1 (*Mrc1*/*Cd206*). In contrast, *Cd36*, *Met*, *Sgms2*, *Fn1*, *Zeb2,* and *Arg2* levels were higher in the late macrophage population, suggesting M2-like polarization.

Therefore, we asked whether these macrophages provide an immunosuppressive microenvironment during *E. faecalis* infection. Cellular interactome analysis revealed enrichment of the ANNEXIN signaling pathway, particularly Anxa1:Fpr1 and Anxa1:Fpr2 ligand-receptor pairs between M2-like macrophage and endothelial or neutrophil cells (**Figure S5I-K**), which inhibits pro-inflammatory cytokine production[67]. Together, these results demonstrate that *E. faecalis* infection influences macrophage polarization towards an anti-inflammatory phenotype. Importantly, the ANXA1:FPR1 interaction has been implicated in the tumor microenvironment of several malignancies[68-71], indicating that the *E. faecalis*-infected wound niche mimics the anti-inflammatory transcriptional program of the tumor microenvironment.

Neutrophils contribute to the anti-inflammatory microenvironment

Our findings revealed an exacerbated inflammatory phenotype during infection (**Figures 2F**, **2G**, **3K**, and **4J**), specifically marked by an abundance of neutrophils[30] (**Figure 1D**). To facilitate a comparison of the broader immune niche, we focused on the neutrophil population, identifying six subpopulations in the integrated dataset (**Figure 5A** and **Table S9**). Among these, clusters 0 and 2 were abundant in the infected condition (**Figures 5B** and **S6A**). The expression of granulocyte colony-stimulating factor receptor (*Csf3r*) and integrin subunit alpha M (*Itgam*/*Cd11b*) was highly expressed across all neutrophils (**Figure 5C**). Furthermore, the higher expression of chemokine (CXC motif) receptor 2 (*Cxcr2*), Fc gamma receptor III (*Fcgr3*/*Cd16*), and ferritin heavy chain (*Fth1*) in clusters 0, 1, 2, 4 and 5 indicated the presence of migrating and maturing neutrophils, regardless of infection status (**Figure 5D**). By contrast, cluster 3 did not express *Cxcr2* and *Fcgr3* and had lower expression of *Fth1* but was enriched in calcium/calmodulin-dependent protein kinase type ID (*Camk1d*), suggesting that this neutrophil subpopulation recruited to the infected wound site might be mature but inactive[72, 73]

The infection-enriched neutrophils demonstrated a functional shift. Cluster 0 with higher expression of *Lrg1,* indicates an activated phagocytic phenotype (**Figure 5E-G**). By contrast, *Csf1*^{hi} neutrophils (cluster 2) were associated with the negative regulation of apoptosis, cytokine production and neutrophil activation. *Csf1* upregulation in neutrophils mediates macrophage differentiation towards an immunotolerant phenotype[74], characterized by low expression of the lymphocyte antigen complex (LY6C) and increased proliferation rate. We then inspected the infected myeloid cells and observed a

higher abundance of the cell proliferation marker, Ki-67 (*Mki67*), and the expression of lymphocyte antigen 6 complex locus 1 (*Ly6c1*). The expression of *Mki67* was specific to terminal macrophage population clusters 2 and 5 (**Figure S5G**) and the level of *Ly6c1* was lower in all macrophages but was specific to LCs (**Figure S5H**). These findings suggest that neutrophils may contribute to the anti-inflammatory polarization of *E. faecalis* infected macrophages.

RNA velocity analysis also estimated infected neutrophils with a propensity to become *Lrg1*^{hi} neutrophils (**Figure 5H**, cluster 0), driven by genes *Entpd1*/*Cd39*, *Picalm*, *Hdc*, *Cytip*, *Sipa1l1* and *Fos* (**Figures 5I**, **S6B** and **S6C**). Moreover, suppression of *Nfkbia* and chemokine ligand-2 (*Cxcl2*) and upregulation of calprotectin (*S100a9*) together indicate an inflammatory response to *E. faecalis* infection (**Figure S6B**). To identify molecular changes that could drive neutrophil state transitions, we sorted the genes based on their peak in pseudo-time, revealing the three distinct neutrophil states: early-stage, intermediate-stage, and late-stage, in the *E. faecalis*-infected wounds (**Figure 5J**). The early response was characterized by *Ccl6*, *Il1f9* (*Il36g*), *Cxcl2*, *S100a6,* and *S100a9*, suggesting an initial pro-inflammatory neutrophil response. By contrast, the late stage demonstrated higher expression of ribosomal proteins (*Rpl5*, *Rpl19* and *Rpl26*), migratory metalloproteinases (*Mmp3*, *Mmp19* and *Adamts5*), and CXC motif ligand-1 (*Cxcl1*), suggesting perturbed neutrophil infiltration. MMP19 has also been implicated in M2 polarization [75], consistent with the anti-inflammatory signatures of the infected macrophage populations (**Figures 4J** and **S5E**). Cellular interactome analysis further predicted the anti-inflammatory status of neutrophils by a strong correlation in the CCL signaling pathway between neutrophils and M2-like macrophages, particularly through the Ccl3:Ccr1 axis (**Figures 5K-M** and **S6D**), an interaction predictive of neutrophil extravasation during *E. faecalis* infection[76]. Neutrophil extravasation is a vital event in immune responses to infections to ensure the survival of the host[7]. In summary, our single-cell analysis of neutrophils during *E. faecalis* wound infection revealed a perturbed pro-inflammatory resolution during infection that may contribute to anti-inflammatory macrophage polarization. Furthermore, our findings uncover prominent differences in immune cell composition in infected wounds, featuring *Lrg1*-rich neutrophil abundance (cluster 0), together with the enrichment of *Arg1*^{hi} M2-like macrophage polarization (clusters 2 and 5). As such, wound healing during *E. faecalis* is characterized by a dysregulated immune response compared to uninfected wounds, which could be associated with delayed healing or chronic infection.

Anti-inflammatory macrophages induce pathogenic angiogenesis

Based on the role of angiogenesis in tissue repair, and our observations of the anti-inflammatory signatures provided by keratinocytes, fibroblasts, and macrophages, we investigated their impact on endothelial cells (ECs). First, we analyzed the two endothelial cell (EC) populations in the integrated dataset and identified 13 clusters with high *Pecam1* and *Plvap* expression. Notably, clusters 0 and 8 were exclusively found in the infected ECs. (**Figures 6A, 6B**, and **S7A-C**). These clusters were involved in ECM deposition, cell differentiation, and development, indicating an anti-inflammatory niche (**Figures 6C** and **6D**). Interestingly, RNA velocity analysis of infected ECs showed a faster velocity in the *Sparc*^{hi} (cluster 0) and *Cilp*^{hi} (cluster 8) cells, suggesting a dynamic transcriptional state (**Figure 6E**). The top lineage driver genes *Malat1*, *Tcf4*, *Rlcb1*, *Diaph2*, *Bmpr2,* and *Adamts9* indicate a pathogenic mechanism in proliferating ECs (**Figure 6F**).

We then explored whether the anti-inflammatory characteristics observed in infected epithelial cells, fibroblasts, and immune cells impacted ECs. To predict these cellular interactions, we conducted a differential NicheNet analysis[77], which involved linking the expression of ligands with corresponding receptors and downstream target gene expressions of these pairs in our scRNA-seq atlas of infected cells. Remarkably, NicheNet analysis revealed Il1b ligand of M2-like macrophages, correlated with the expression of target genes such as biglycan (*Bgn*), *Cd14*, *Ccl3*, *Csf3r*, *Itgam* and *Tnf* in ECs (**Figures 6G** and **S7D**), in line with previous studies[54, 78]. Notably, BGN, a proteoglycan, has been associated with tumor EC signatures[79, 80], further supporting the anti-inflammatory role of M2-like macrophages observed in the infected dataset. Moreover, the infection-induced expression of *Cd14* in EC suggests Toll-like receptor (TLR) activation[81, 82]. Cell-cell interaction analysis also predicted that the Ptgs2, Spp1 and Il1a ligand activity in M2-like macrophages influenced the expression of target genes such as calprotectin (*S100a8* and *S100a9*) and colony-stimulating factor 3 (*Csf3*) These interactions suggest a potential disruption of EC integrity in the presence of *E. faecalis* infection. Similarly, according to the CellChat analysis, ECs exhibited activation of the SPP1 and CXCL signaling pathways (**Figures 6H-J**, **S7E** and **S7F**). Expression of the ligands Spp1, Cxcl2 and Cxcl3 were abundant in keratinocytes, fibroblasts, and M2-like macrophages during the infection (**Figure 6J**). In the uninfected ECs, however, fibroblasts modulated the expression of target genes such as TEK tyrosine kinase (*Tek*), Forkhead box

protein O1 (*Foxo1*) and selectin-E (*Sele*), with notable angiopoietin 1 activity (**Figure S7D**), pointing to normal endothelial cell activity.

During unperturbed wound healing, macrophages modulate angiogenesis by producing proteases, including matrix metalloproteinases (MMPs), which help degrade the extracellular matrix in the wound bed. Additionally, macrophages secrete chemotactic factors such as TNF-α, VEGF and TGF-β to promote the EC migration[83, 84]. Furthermore, the TGF-β signaling pathway induces fibroblast proliferation and ECM production in wound healing[85, 86]. Our analysis of the cellular interactome in the uninfected wound dataset revealed strong interactions in the TGF-β and VEGF signaling pathways (**Figure S7H-I**), corroborating previous studies[5, 54]. These findings suggest that uninfected wounds undergo reparative angiogenesis while *E. faecalis* infection evokes pathological vascularization. Overall, our analysis underlines the M2-like macrophage-EC interactions as targets of altered cell-cell signaling during bacteria-infected wound healing.

DISCUSSION

Wound healing is an intricate process that involves the cooperation of various cellular and extracellular components. Disruptions to this network can perturb the healing dynamics. Previous scRNA-seq studies have primarily focused on the transcriptional profiles of epithelial and fibroblast populations in wound healing[3-5, 53, 55]. However, the impact of the host-pathogen interactions on wound healing transcriptional programs remains to be investigated. Here, our work presents the first comprehensive single-cell atlas of mouse skin wounds following infection, highlighting the transcriptional aberration in wound healing. *E. faecalis* has immunosuppressive activity in various tissues and infection sites[15, 17Kao, 2023 #134, 30]. By surveying approximately 23,000 cells, we identified cell types, characterized shared and distinct transcriptional programs, and delineated terminal phenotypes and signaling pathways in homeostatic healing or bacterial wound infections. These scRNA-seq findings elucidate the immunosuppressive role of *E. faecalis* during wound infections, providing valuable insights into the underlying mechanisms.

To explore the cellular landscape of *E. faecalis*-infected wounds and the impact of infection on wound healing, we focused on cell types specifically enriched in these tissues. Our analysis revealed infection-

activated transcriptional states in keratinocytes, fibroblasts, and immune cells. The presence of clusters 0 and 6, exclusive to the epithelial dataset, along with RNA velocity analysis pointing to *Zeb2*-expressing cells (**Figure 2I**), suggests a potential role of *E. faecalis* in promoting a partial EMT in keratinocytes. We also identified a terminal keratinocyte population (cluster 2) at 4 dpi, characterized by the consumption of *Krt77* and *Krtdap* over pseudo-time, confirming terminal keratinocyte differentiation (**Figures 2I and S2C**). By contrast, uninfected wounds showed proliferating keratinocyte (*Mki67*^{hi}) and hair follicle (*Lrg5*^{hi}) cells (**Figure 2H**), consistent with previous findings on wound healing and skin maintenance signatures[3, 4]. Furthermore, we found two infection-specific fibroblast populations enriched in *Lyz2*/*Tagln* and *Timp1*, identifying their myofibroblast characteristics. The RNA velocity analysis confirmed cluster 5 as the terminal fibroblast population derived from myofibroblasts (cluster 2) (**Figure 3I**). Additionally, an increase in *Timp1* expression correlated with cell growth and proliferation signatures (*Sparc*, *Fgf7* and *Malat1*) over latent time in cluster 5 (**Figures S4C and S4D**). These findings collectively demonstrate a profibrotic state in fibroblasts driven by *E. faecalis*-induced transcriptional dynamics.

To investigate the impact of immunosuppressive signatures in keratinocytes and fibroblasts, we examined how *E. faecalis* infection influenced the immune response in wounds. Given that prolonged macrophage survival is associated with impaired wound healing[87, 88], we primarily focused on the macrophage populations. We identified subpopulations of M2-like macrophages expressing *Arg1*, *Ptgs2* and *Sparc* genes (**Figure 4F-I**). COX-2 (cyclooxygenase-2, encoded by *Ptgs2* gene) has been reported as a crucial regulator of M2-like polarization in tumor-associated macrophages[89, 90]. While macrophage polarization is complex in humans and other higher organisms[91, 92], our scRNA-seq data suggests that *E. faecalis* infection drives an anti-inflammatory microenvironment resembling the tumor microenvironment. These findings confirm and expand on previous studies highlighting the immunosuppressive role of *E. faecalis* in different contexts[15, 17, 30].

Our findings also elaborate on the potential cell-cell communication and signaling pathways involved in wound healing. Ligand-receptor interaction analysis revealed an immune-suppressive ecosystem driven by M2-like macrophages during bacterial infection (**Figure 6G**). CellChat analysis confirmed that M2-like macrophages play a crucial role in regulating angiogenesis through the Vegfa:Vegfr1 ligand-

receptor pair (**Figures 6H**, **6I**, **S7E**, **S7F**, and **Table S6**). Further, the Spp1 ligand correlated with integrins (Itgav+Itgb1, Itgav+Itgb3, Itga5+Itgb1) and the cluster of differentiation receptor Cd44 in ECs. Notably, while the Spp1 ligand of macrophages registered strong interactions with ECs, infected keratinocytes and fibroblasts were identified as the primary sources of Spp1 ligand. The infection-specific abundance of *Spp1* in these clusters highlight a partial EMT state in our extended analyses (**Figures 2E-I**). Furthermore, the interaction between Spp1 and Cd44 in M2-like macrophages and ECs indicated a proliferative state. The neutrophil chemokine *Cxcl2*, which promotes wound healing and angiogenesis[93, 94], strongly correlated with the atypical chemokine receptor *Ackr1*, suggesting neutrophil extravasation. Additionally, the secretion of heparin-binding epidermal growth factor (*Hbegf*) by keratinocytes and epiregulin-enriched fibroblasts (*Ereg*^{hi}) further confirmed the presence of an anti-inflammatory microenvironment and angiogenic ECs in bacteria-infected wounds (**Figures 6H**, **6I**, and **S7F**).

In summary, our study provides insights into the cellular landscape, transcriptional programs, and signaling pathways associated with uninfected and *E. faecalis*-infected skin wounds. We confirm the immune-suppressive role of *E. faecalis* in wound healing, consistent with previous findings in different experimental settings[17Kao, 2023 #134, 30]} Importantly, we identify specific ligand-receptor pairs and signaling pathways affected during wound infection. The increased number of predicted signaling interactions suggests that *E. faecalis* modulates cellular communication to alter the immune response. Notably, the CXCL/SPP1 signaling pathway emerges as a critical player in shaping the immune-altering ecosystem during wound healing, highlighting its potential as a therapeutic target for chronic infections. Collectively, our findings demonstrate the collaborative role of keratinocytes, fibroblasts, and immune cells in immune suppression through CXCL/SPP1 signaling, providing new avenues for the treatment of chronic wound infections.

LIMITATIONS OF THE STUDY

Our study provides a comprehensive comparison of the transcriptomic and cellular communication profiles between uninfected and *E. faecalis*-infected full-thickness mouse skin wounds at four days post-infection. However, our study lacks a reference dataset of uninfected, unwounded dorsal skin transcriptome, which would have allowed us to investigate transcriptomic changes temporally,

especially induced by the wounding alone. Although we explored public datasets to address this limitation [53, 54], the low number of cells in public datasets, particularly for macrophage populations (data not shown), prevented their inclusion in our analysis. Additionally, the absence of multiple time points hinders our ability to examine temporal changes and the dynamic kinetics of host responses following infection.

ACKNOWLEDGEMENTS

We are grateful to Drs. Claudia Stocks and Sophie Janssens for helpful discussions and critical reading of the manuscript. We thank the Singapore Centre for Environmental Life Sciences Engineering High Throughput Sequencing Unit for providing us with the Chromium Controller (10X Genomics) microfluidic partitioning instrument for single-cell encapsulation. The computational work for this article was partially performed on resources of the National Supercomputing Centre (NSCC), Singapore. This work was supported by funds from the National Medical Research Council Open Fund (MOH-000566 to K.A.K. and G.T. and MOH-000645 to K.A.K.), the Singapore Ministry of Education Academic Research Fund Tier 2 (MOE2019-T2-2-089 to K.A.K.), NTU Research Scholarship to S.Y.T.L. (predoctoral fellowship), and Nanyang President's Graduate Scholarship to F.R.T. Parts of this work were also supported by the National Research Foundation and Ministry of Education Singapore under its Research Centre of Excellence Program (SCELSE).

AUTHOR CONTRIBUTIONS

Conceptualization, C.C., K.A.K. and G.T.; Methodology, C.C., F.R.T., K.A.K. and G.T.; Software, C.C.; Validation, C.C.; Formal Analysis, C.C. and F.R.T.; Investigation, C.C., S.Y.T.L., F.R.T., and M.V.; Resources, C.C. and M.V., Data Curation, C.C.; Writing – Original Draft; C.C., K.A.K., and G.T.; Writing – Review & Editing, S.Y.T.L., F.R.T, K.A.K., and G.T.; Visualization, C.C. and G.T.; Supervision, K.A.K. and G.T.; Project Administration, K.A.K. and G.T.; Funding Acquisition, K.A.K. and G.T.

DECLARATION OF INTERESTS

The authors declare no competing financial interests.

Table S1. Number of cells in each Louvain cluster grouped by condition. Related to Figure 1.

Table S2. Differential expression table of genes for the main class clusters. Related to Figure 1C.

Table S3. Differential expression table of genes for the main uninfected class clusters. Related to Figure 1C.

Table S4. Differential expression table of genes for the main infected class clusters. Related to Figure 1C.

Table S5. Differential expression table of genes for sub-clustered keratinocytes. Related to Figure 2.

Table S6. CellChat comparison for ligand:receptor pairs for the uninfected and infected datasets. Related to Figures 2-6.

Table S7. Differential expression table of genes for sub-clustered fibroblasts. Related to Figure 3.

Table S8. Differential expression table of genes for sub-clustered myeloid clusters. Related to Figure 4.

Table S9. Differential expression table of genes for sub-clustered neutrophil clusters. Related to Figure 5.

REFERENCES

1. Cheng JB, Sedgewick AJ, Finnegan AI, Harirchian P, Lee J, Kwon S, et al. Transcriptional Programming of Normal and Inflamed Human Epidermis at Single-Cell Resolution. Cell Rep. 2018;25(4):871-83. doi: 10.1016/j.celrep.2018.09.006. PubMed PMID: 30355494; PubMed Central PMCID: PMCPMC6367716.
2. Der E, Suryawanshi H, Morozov P, Kustagi M, Goilav B, Ranabothu S, et al. Tubular cell and keratinocyte single-cell transcriptomics applied to lupus nephritis reveal type I IFN and fibrosis relevant pathways. Nat Immunol. 2019;20(7):915-27. Epub 20190520. doi: 10.1038/s41590-019-0386-1. PubMed PMID: 31110316; PubMed Central PMCID: PMCPMC6584054.
3. Joost S, Annusver K, Jacob T, Sun X, Dalessandri T, Sivan U, et al. The Molecular Anatomy of Mouse Skin during Hair Growth and Rest. Cell Stem Cell. 2020;26(3):441-57 e7. Epub 20200227. doi: 10.1016/j.stem.2020.01.012. PubMed PMID: 32109378.
4. Joost S, Jacob T, Sun X, Annusver K, La Manno G, Sur I, et al. Single-Cell Transcriptomics of Traced Epidermal and Hair Follicle Stem Cells Reveals Rapid Adaptations during Wound Healing. Cell Rep. 2018;25(3):585-97 e7. doi: 10.1016/j.celrep.2018.09.059. PubMed PMID: 30332640.
5. Joost S, Zeisel A, Jacob T, Sun X, La Manno G, Lonnerberg P, et al. Single-Cell Transcriptomics Reveals that Differentiation and Spatial Signatures Shape Epidermal and Hair Follicle Heterogeneity. Cell Syst. 2016;3(3):221-37 e9. Epub 20160915. doi: 10.1016/j.cels.2016.08.010. PubMed PMID: 27641957; PubMed Central PMCID: PMCPMC5052454.
6. Philippeos C, Telerman SB, Oules B, Pisco AO, Shaw TJ, Elgueta R, et al. Spatial and Single-Cell Transcriptional Profiling Identifies Functionally Distinct Human Dermal Fibroblast Subpopulations. J Invest Dermatol. 2018;138(4):811-25. Epub 20180131. doi: 10.1016/j.jid.2018.01.016. PubMed PMID: 29391249; PubMed Central PMCID: PMCPMC5869055.
7. Theocharidis G, Rahmani S, Lee S, Li Z, Lobao A, Kounas K, et al. Murine macrophages or their secretome delivered in alginate dressings enhance impaired wound healing in diabetic mice. Biomaterials. 2022;288:121692. Epub 2022/08/08. doi: 10.1016/j.biomaterials.2022.121692. PubMed PMID: 35934520; PubMed Central PMCID: PMCPMC9977170.
8. Eming SA, Martin P, Tomic-Canic M. Wound repair and regeneration: mechanisms, signaling, and translation. Sci Transl Med. 2014;6(265):265sr6. doi: 10.1126/scitranslmed.3009337. PubMed PMID: 25473038; PubMed Central PMCID: PMCPMC4973620.
9. Masson-Meyers DS, Andrade TAM, Caetano GF, Guimaraes FR, Leite MN, Leite SN, et al. Experimental models and methods for cutaneous wound healing assessment. Int J Exp Pathol. 2020;101(1-2):21-37. Epub 20200330. doi: 10.1111/iep.12346. PubMed PMID: 32227524; PubMed Central PMCID: PMCPMC7306904.
10. Minutti CM, Knipper JA, Allen JE, Zaiss DM. Tissue-specific contribution of macrophages to wound healing. Semin Cell Dev Biol. 2017;61:3-11. Epub 20160810. doi: 10.1016/j.semcdb.2016.08.006. PubMed PMID: 27521521.
11. Rognoni E, Watt FM. Skin Cell Heterogeneity in Development, Wound Healing, and Cancer. Trends Cell Biol. 2018;28(9):709-22. Epub 20180525. doi: 10.1016/j.tcb.2018.05.002. PubMed PMID: 29807713; PubMed Central PMCID: PMCPMC6098245.
12. Lindley LE, Stojadinovic O, Pastar I, Tomic-Canic M. Biology and Biomarkers for Wound Healing. Plast Reconstr Surg. 2016;138(3 Suppl):18S-28S. doi: 10.1097/PRS.0000000000002682. PubMed PMID: 27556760; PubMed Central PMCID: PMCPMC4998971.
13. Wang PH, Huang BS, Horng HC, Yeh CC, Chen YJ. Wound healing. J Chin Med Assoc. 2018;81(2):94-101. Epub 20171121. doi: 10.1016/j.jcma.2017.11.002. PubMed PMID: 29169897.
14. Ashcroft KJ, Syed F, Bayat A. Site-specific keloid fibroblasts alter the behaviour of normal skin and normal scar fibroblasts through paracrine signalling. PLoS One. 2013;8(12):e75600. Epub 20131209. doi: 10.1371/journal.pone.0075600. PubMed PMID: 24348987; PubMed Central PMCID: PMCPMC3857170.
15. Kao PHN, Kline KA. Dr. Jekyll and Mr. Hide: How Enterococcus faecalis Subverts the Host Immune Response to Cause Infection. J Mol Biol. 2019;431(16):2932-45. Epub 20190525. doi: 10.1016/j.jmb.2019.05.030. PubMed PMID: 31132360.
16. Ch'ng JH, Chong KKL, Lam LN, Wong JJ, Kline KA. Biofilm-associated infection by enterococci. Nat Rev Microbiol. 2019;17(2):82-94. doi: 10.1038/s41579-018-0107-z. PubMed PMID: 30337708.
17. Tien BYQ, Goh HMS, Chong KKL, Bhaduri-Tagore S, Holec S, Dress R, et al. Enterococcus faecalis Promotes Innate Immune Suppression and Polymicrobial Catheter-Associated Urinary Tract Infection. Infect Immun. 2017;85(12). Epub 20171117. doi: 10.1128/IAI.00378-17. PubMed PMID: 28893918; PubMed Central PMCID: PMCPMC5695114.

18. Kao PH, Ch'ng JH, Chong KKL, Stocks CJ, Wong SL, Kline KA. Enterococcus faecalis suppresses Staphylococcus aureus-induced NETosis and promotes bacterial survival in polymicrobial infections. FEMS Microbes. 2023;4:xtad019. Epub 2023/10/30. doi: 10.1093/femsmc/xtad019. PubMed PMID: 37900578; PubMed Central PMCID: PMCPMC10608956.
19. Horsley H, Dharmasena D, Malone-Lee J, Rohn JL. A urine-dependent human urothelial organoid offers a potential alternative to rodent models of infection. Sci Rep. 2018;8(1):1238. Epub 20180119. doi: 10.1038/s41598-018-19690-7. PubMed PMID: 29352171; PubMed Central PMCID: PMCPMC5775255.
20. Horsley H, Malone-Lee J, Holland D, Tuz M, Hibbert A, Kelsey M, et al. Enterococcus faecalis subverts and invades the host urothelium in patients with chronic urinary tract infection. PLoS One. 2013;8(12):e83637. Epub 20131210. doi: 10.1371/journal.pone.0083637. PubMed PMID: 24363814; PubMed Central PMCID: PMCPMC3868479.
21. Bertuccini L, Ammendolia MG, Superti F, Baldassarri L. Invasion of HeLa cells by Enterococcus faecalis clinical isolates. Med Microbiol Immunol. 2002;191(1):25-31. doi: 10.1007/s00430-002-0115-4. PubMed PMID: 12137196.
22. Olmsted SB, Dunny GM, Erlandsen SL, Wells CL. A plasmid-encoded surface protein on Enterococcus faecalis augments its internalization by cultured intestinal epithelial cells. J Infect Dis. 1994;170(6):1549-56. doi: 10.1093/infdis/170.6.1549. PubMed PMID: 7995995.
23. Wells CL, Jechorek RP, Erlandsen SL. Evidence for the translocation of Enterococcus faecalis across the mouse intestinal tract. J Infect Dis. 1990;162(1):82-90. doi: 10.1093/infdis/162.1.82. PubMed PMID: 2113080.
24. Wells CL, Jechorek RP, Maddaus MA, Simmons RL. Effects of clindamycin and metronidazole on the intestinal colonization and translocation of enterococci in mice. Antimicrob Agents Chemother. 1988;32(12):1769-75. doi: 10.1128/AAC.32.12.1769. PubMed PMID: 3245692; PubMed Central PMCID: PMCPMC176015.
25. Zou J, Shankar N. The opportunistic pathogen Enterococcus faecalis resists phagosome acidification and autophagy to promote intracellular survival in macrophages. Cell Microbiol. 2016;18(6):831-43. Epub 20160112. doi: 10.1111/cmi.12556. PubMed PMID: 26663775.
26. Zou J, Shankar N. Enterococcus faecalis infection activates phosphatidylinositol 3-kinase signaling to block apoptotic cell death in macrophages. Infect Immun. 2014;82(12):5132-42. Epub 20140929. doi: 10.1128/IAI.02426-14. PubMed PMID: 25267834; PubMed Central PMCID: PMCPMC4249289.
27. Gentry-Weeks CR, Karkhoff-Schweizer R, Pikis A, Estay M, Keith JM. Survival of Enterococcus faecalis in mouse peritoneal macrophages. Infect Immun. 1999;67(5):2160-5. doi: 10.1128/IAI.67.5.2160-2165.1999. PubMed PMID: 10225869; PubMed Central PMCID: PMCPMC115952.
28. da Silva RAG, Tay WH, Ho FK, Tanoto FR, Chong KKL, Choo PY, et al. Enterococcus faecalis alters endo-lysosomal trafficking to replicate and persist within mammalian cells. PLoS Pathog. 2022;18(4):e1010434. Epub 20220407. doi: 10.1371/journal.ppat.1010434. PubMed PMID: 35390107; PubMed Central PMCID: PMCPMC9017951.
29. Nunez N, Derre-Bobillot A, Trainel N, Lakisic G, Lecomte A, Mercier-Nome F, et al. The unforeseen intracellular lifestyle of Enterococcus faecalis in hepatocytes. Gut Microbes. 2022;14(1):2058851. doi: 10.1080/19490976.2022.2058851. PubMed PMID: 35373699; PubMed Central PMCID: PMCPMC8986240.
30. Chong KKL, Tay WH, Janela B, Yong AMH, Liew TH, Madden L, et al. Enterococcus faecalis Modulates Immune Activation and Slows Healing During Wound Infection. J Infect Dis. 2017;216(12):1644-54. doi: 10.1093/infdis/jix541. PubMed PMID: 29045678; PubMed Central PMCID: PMCPMC5854026.
31. Tan CAZL, Ling Ning
Biukovic, Goran
Soh, Eliza Ye-Chen
Toh, Xiao Wei
Lemos, Jose A.
Kline, Kimberly A. Enterococcus faecalis antagonizes Pseudomonas aeruginosa growth in polymicrobial biofilms. bioRxiv. 2022.
32. Rashid R, Nair ZJ, Chia DMH, Chong KKL, Cazenave Gassiot A, Morley SA, et al. Depleting Cationic Lipids Involved in Antimicrobial Resistance Drives Adaptive Lipid Remodeling in Enterococcus faecalis. mBio. 2023;14(1):e0307322. Epub 20230111. doi: 10.1128/mbio.03073-22. PubMed PMID: 36629455; PubMed Central PMCID: PMCPMC9973042.

33. Kandaswamy K, Liew TH, Wang CY, Huston-Warren E, Meyer-Hoffert U, Hultenby K, et al. Focal targeting by human beta-defensin 2 disrupts localized virulence factor assembly sites in Enterococcus faecalis. Proc Natl Acad Sci U S A. 2013;110(50):20230-5. Epub 20131104. doi: 10.1073/pnas.1319066110. PubMed PMID: 24191013; PubMed Central PMCID: PMCPMC3864318.
34. Bao Y, Sakinc T, Laverde D, Wobser D, Benachour A, Theilacker C, et al. Role of mprF1 and mprF2 in the pathogenicity of Enterococcus faecalis. PLoS One. 2012;7(6):e38458. Epub 20120618. doi: 10.1371/journal.pone.0038458. PubMed PMID: 22723861; PubMed Central PMCID: PMCPMC3377626.
35. Jin S, Guerrero-Juarez CF, Zhang L, Chang I, Ramos R, Kuan CH, et al. Inference and analysis of cell-cell communication using CellChat. Nat Commun. 2021;12(1):1088. Epub 2021/02/19. doi: 10.1038/s41467-021-21246-9. PubMed PMID: 33597522; PubMed Central PMCID: PMCPMC7889871.
36. Schultz G, Rotatori DS, Clark W. EGF and TGF-alpha in wound healing and repair. J Cell Biochem. 1991;45(4):346-52. doi: 10.1002/jcb.240450407. PubMed PMID: 2045428.
37. Guasch G, Schober M, Pasolli HA, Conn EB, Polak L, Fuchs E. Loss of TGFbeta signaling destabilizes homeostasis and promotes squamous cell carcinomas in stratified epithelia. Cancer Cell. 2007;12(4):313-27. doi: 10.1016/j.ccr.2007.08.020. PubMed PMID: 17936557; PubMed Central PMCID: PMCPMC2424201.
38. Li X, Zhai Y, Xi B, Ma W, Zhang J, Ma X, et al. Pinocembrin Ameliorates Skin Fibrosis via Inhibiting TGF-beta1 Signaling Pathway. Biomolecules. 2021;11(8). Epub 20210819. doi: 10.3390/biom11081240. PubMed PMID: 34439906; PubMed Central PMCID: PMCPMC8393190.
39. Xie Y, Gao K, Hakkinen L, Larjava HS. Mice lacking beta6 integrin in skin show accelerated wound repair in dexamethasone impaired wound healing model. Wound Repair Regen. 2009;17(3):326-39. doi: 10.1111/j.1524-475X.2009.00480.x. PubMed PMID: 19660040.
40. Zappia L, Oshlack A. Clustering trees: a visualization for evaluating clusterings at multiple resolutions. Gigascience. 2018;7(7). Epub 2018/07/17. doi: 10.1093/gigascience/giy083. PubMed PMID: 30010766; PubMed Central PMCID: PMCPMC6057528.
41. Franzen O, Gan LM, Bjorkegren JLM. PanglaoDB: a web server for exploration of mouse and human single-cell RNA sequencing data. Database (Oxford). 2019;2019. Epub 2019/04/06. doi: 10.1093/database/baz046. PubMed PMID: 30951143; PubMed Central PMCID: PMCPMC6450036.
42. Hofer F, Di Sario G, Musiu C, Sartoris S, De Sanctis F, Ugel S. A Complex Metabolic Network Confers Immunosuppressive Functions to Myeloid-Derived Suppressor Cells (MDSCs) within the Tumour Microenvironment. Cells. 2021;10(10). Epub 20211009. doi: 10.3390/cells10102700. PubMed PMID: 34685679; PubMed Central PMCID: PMCPMC8534848.
43. Veglia F, Sanseviero E, Gabrilovich DI. Myeloid-derived suppressor cells in the era of increasing myeloid cell diversity. Nat Rev Immunol. 2021;21(8):485-98. Epub 20210201. doi: 10.1038/s41577-020-00490-y. PubMed PMID: 33526920; PubMed Central PMCID: PMCPMC7849958.
44. La Manno G, Soldatov R, Zeisel A, Braun E, Hochgerner H, Petukhov V, et al. RNA velocity of single cells. Nature. 2018;560(7719):494-8. Epub 2018/08/10. doi: 10.1038/s41586-018-0414-6. PubMed PMID: 30089906; PubMed Central PMCID: PMCPMC6130801.
45. Lange M, Bergen V, Klein M, Setty M, Reuter B, Bakhti M, et al. CellRank for directed single-cell fate mapping. Nat Methods. 2022;19(2):159-70. Epub 20220113. doi: 10.1038/s41592-021-01346-6. PubMed PMID: 35027767; PubMed Central PMCID: PMCPMC8828480.
46. Standal T, Borset M, Sundan A. Role of osteopontin in adhesion, migration, cell survival and bone remodeling. Exp Oncol. 2004;26(3):179-84. PubMed PMID: 15494684.
47. Denhardt DT, Noda M, O'Regan AW, Pavlin D, Berman JS. Osteopontin as a means to cope with environmental insults: regulation of inflammation, tissue remodeling, and cell survival. J Clin Invest. 2001;107(9):1055-61. doi: 10.1172/JCI12980. PubMed PMID: 11342566; PubMed Central PMCID: PMCPMC209291.
48. Guerrero-Juarez CF, Dedhia PH, Jin S, Ruiz-Vega R, Ma D, Liu Y, et al. Single-cell analysis reveals fibroblast heterogeneity and myeloid-derived adipocyte progenitors in murine skin wounds. Nat Commun. 2019;10(1):650. Epub 20190208. doi: 10.1038/s41467-018-08247-x. PubMed PMID: 30737373; PubMed Central PMCID: PMCPMC6368572.
49. Gao W, Liu D, Sun H, Shao Z, Shi P, Li T, et al. SPP1 is a prognostic related biomarker and correlated with tumor-infiltrating immune cells in ovarian cancer. BMC Cancer. 2022;22(1):1367. Epub 2022/12/31. doi: 10.1186/s12885-022-10485-8. PubMed PMID: 36585688; PubMed Central PMCID: PMCPMC9805166.

50. Cheng M, Liang G, Yin Z, Lin X, Sun Q, Liu Y. Immunosuppressive role of SPP1-CD44 in the tumor microenvironment of intrahepatic cholangiocarcinoma assessed by single-cell RNA sequencing. J Cancer Res Clin Oncol. 2023;149(9):5497-512. Epub 2022/12/06. doi: 10.1007/s00432-022-04498-w. PubMed PMID: 36469154.
51. Farr L, Ghosh S, Moonah S. Role of MIF Cytokine/CD74 Receptor Pathway in Protecting Against Injury and Promoting Repair. Front Immunol. 2020;11:1273. Epub 20200623. doi: 10.3389/fimmu.2020.01273. PubMed PMID: 32655566; PubMed Central PMCID: PMCPMC7325688.
52. Jager B, Klatt D, Plappert L, Golpon H, Lienenklaus S, Barbosa PD, et al. CXCR4/MIF axis amplifies tumor growth and epithelial-mesenchymal interaction in non-small cell lung cancer. Cell Signal. 2020;73:109672. Epub 20200516. doi: 10.1016/j.cellsig.2020.109672. PubMed PMID: 32428553.
53. Haensel D, Jin S, Sun P, Cinco R, Dragan M, Nguyen Q, et al. Defining Epidermal Basal Cell States during Skin Homeostasis and Wound Healing Using Single-Cell Transcriptomics. Cell Rep. 2020;30(11):3932-47 e6. doi: 10.1016/j.celrep.2020.02.091. PubMed PMID: 32187560; PubMed Central PMCID: PMCPMC7218802.
54. Vu R, Jin S, Sun P, Haensel D, Nguyen QH, Dragan M, et al. Wound healing in aged skin exhibits systems-level alterations in cellular composition and cell-cell communication. Cell Rep. 2022;40(5):111155. doi: 10.1016/j.celrep.2022.111155. PubMed PMID: 35926463; PubMed Central PMCID: PMCPMC9901190.
55. Deng CC, Hu YF, Zhu DH, Cheng Q, Gu JJ, Feng QL, et al. Single-cell RNA-seq reveals fibroblast heterogeneity and increased mesenchymal fibroblasts in human fibrotic skin diseases. Nat Commun. 2021;12(1):3709. Epub 20210617. doi: 10.1038/s41467-021-24110-y. PubMed PMID: 34140509; PubMed Central PMCID: PMCPMC8211847.
56. Fang T, Zhang L, Yin X, Wang Y, Zhang X, Bian X, et al. The prognostic marker elastin correlates with epithelial-mesenchymal transition and vimentin-positive fibroblasts in gastric cancer. J Pathol Clin Res. 2023;9(1):56-72. Epub 20221013. doi: 10.1002/cjp2.298. PubMed PMID: 36226731; PubMed Central PMCID: PMCPMC9732685.
57. Fitzgerald AA, Weiner LM. The role of fibroblast activation protein in health and malignancy. Cancer Metastasis Rev. 2020;39(3):783-803. doi: 10.1007/s10555-020-09909-3. PubMed PMID: 32601975; PubMed Central PMCID: PMCPMC7487063.
58. Gornicki T, Lambrinow J, Mrozowska M, Podhorska-Okolow M, Dziegiel P, Grzegrzolka J. Role of RBMS3 Novel Potential Regulator of the EMT Phenomenon in Physiological and Pathological Processes. Int J Mol Sci. 2022;23(18). Epub 20220917. doi: 10.3390/ijms231810875. PubMed PMID: 36142783; PubMed Central PMCID: PMCPMC9503485.
59. Mizumoto S, Janecke AR, Sadeghpour A, Povysil G, McDonald MT, Unger S, et al. CSGALNACT1-congenital disorder of glycosylation: A mild skeletal dysplasia with advanced bone age. Hum Mutat. 2020;41(3):655-67. Epub 20191203. doi: 10.1002/humu.23952. PubMed PMID: 31705726; PubMed Central PMCID: PMCPMC7027858.
60. Landen NX, Li D, Stahle M. Transition from inflammation to proliferation: a critical step during wound healing. Cell Mol Life Sci. 2016;73(20):3861-85. Epub 20160514. doi: 10.1007/s00018-016-2268-0. PubMed PMID: 27180275; PubMed Central PMCID: PMCPMC5021733.
61. Mattila JT, Ojo OO, Kepka-Lenhart D, Marino S, Kim JH, Eum SY, et al. Microenvironments in tuberculous granulomas are delineated by distinct populations of macrophage subsets and expression of nitric oxide synthase and arginase isoforms. J Immunol. 2013;191(2):773-84. Epub 2013/06/12. doi: 10.4049/jimmunol.1300113. PubMed PMID: 23749634; PubMed Central PMCID: PMCPMC3746594.
62. Cuervo H, Guerrero NA, Carbajosa S, Beschin A, De Baetselier P, Girones N, et al. Myeloid-derived suppressor cells infiltrate the heart in acute Trypanosoma cruzi infection. J Immunol. 2011;187(5):2656-65. Epub 2011/08/02. doi: 10.4049/jimmunol.1002928. PubMed PMID: 21804013.
63. Maloney J, Keselman A, Li E, Singer SM. Macrophages expressing arginase 1 and nitric oxide synthase 2 accumulate in the small intestine during Giardia lamblia infection. Microbes Infect. 2015;17(6):462-7. Epub 2015/03/24. doi: 10.1016/j.micinf.2015.03.006. PubMed PMID: 25797399; PubMed Central PMCID: PMCPMC4461514.
64. Munadziroh E, Askandar MG, Yuliati A, Surboyo MDC, Wan Harun WHA. The effect of secretory leukocyte protease inhibitor amnion membrane on incisional wound healing. J Oral Biol Craniofac Res. 2022;12(3):358-62. Epub 20220422. doi: 10.1016/j.jobcr.2022.04.001. PubMed PMID: 35514674; PubMed Central PMCID: PMCPMC9062474.

65. Recalcati S, Gammella E, Buratti P, Doni A, Anselmo A, Locati M, et al. Macrophage ferroportin is essential for stromal cell proliferation in wound healing. Haematologica. 2019;104(1):47-58. Epub 20180816. doi: 10.3324/haematol.2018.197517. PubMed PMID: 30115660; PubMed Central PMCID: PMCPMC6312033.
66. Hu J, Ma Y, Ma J, Chen S, Zhang X, Guo S, et al. Macrophage-derived SPARC Attenuates M2-mediated Pro-tumour Phenotypes. J Cancer. 2020;11(10):2981-92. Epub 20200304. doi: 10.7150/jca.39651. PubMed PMID: 32226513; PubMed Central PMCID: PMCPMC7086259.
67. Yang YH, Aeberli D, Dacumos A, Xue JR, Morand EF. Annexin-1 regulates macrophage IL-6 and TNF via glucocorticoid-induced leucine zipper. J Immunol. 2009;183(2):1435-45. Epub 2009/06/26. doi: 10.4049/jimmunol.0804000. PubMed PMID: 19553536.
68. Zhao L, Wang W, Niu P, Luan X, Zhao D, Chen Y. The molecular mechanisms of CTHRC1 in gastric cancer by integrating TCGA, GEO and GSA datasets. Front Genet. 2022;13:900124. Epub 20220719. doi: 10.3389/fgene.2022.900124. PubMed PMID: 35928443; PubMed Central PMCID: PMCPMC9343808.
69. Vecchi L, Alves Pereira Zoia M, Goss Santos T, de Oliveira Beserra A, Colaco Ramos CM, Franca Matias Colombo B, et al. Inhibition of the AnxA1/FPR1 autocrine axis reduces MDA-MB-231 breast cancer cell growth and aggressiveness in vitro and in vivo. Biochim Biophys Acta Mol Cell Res. 2018;1865(9):1368-82. Epub 20180620. doi: 10.1016/j.bbamcr.2018.06.010. PubMed PMID: 29932988.
70. Takaoka RTC, Sertorio ND, Magalini LPJ, Dos Santos LM, Souza HR, Iyomasa-Pilon MM, et al. Expression profiles of Annexin A1, formylated peptide receptors and cyclooxigenase-2 in gastroesophageal inflammations and neoplasias. Pathol Res Pract. 2018;214(2):181-6. Epub 20171207. doi: 10.1016/j.prp.2017.12.003. PubMed PMID: 29254791.
71. Cheng TY, Wu MS, Lin JT, Lin MT, Shun CT, Hua KT, et al. Formyl Peptide receptor 1 expression is associated with tumor progression and survival in gastric cancer. Anticancer Res. 2014;34(5):2223-9. PubMed PMID: 24778024.
72. Evrard M, Kwok IWH, Chong SZ, Teng KWW, Becht E, Chen J, et al. Developmental Analysis of Bone Marrow Neutrophils Reveals Populations Specialized in Expansion, Trafficking, and Effector Functions. Immunity. 2018;48(2):364-79 e8. Epub 2018/02/22. doi: 10.1016/j.immuni.2018.02.002. PubMed PMID: 29466759.
73. Chen J, Bai Y, Xue K, Li Z, Zhu Z, Li Q, et al. CREB1-driven CXCR4(hi) neutrophils promote skin inflammation in mouse models and human patients. Nat Commun. 2023;14(1):5894. Epub 2023/09/22. doi: 10.1038/s41467-023-41484-3. PubMed PMID: 37736772; PubMed Central PMCID: PMCPMC10516899.
74. Braza MS, Conde P, Garcia M, Cortegano I, Brahmachary M, Pothula V, et al. Neutrophil derived CSF1 induces macrophage polarization and promotes transplantation tolerance. Am J Transplant. 2018;18(5):1247-55. Epub 20180207. doi: 10.1111/ajt.14645. PubMed PMID: 29314558; PubMed Central PMCID: PMCPMC5910259.
75. Fingleton B. Matrix metalloproteinases as regulators of inflammatory processes. Biochim Biophys Acta Mol Cell Res. 2017;1864(11 Pt A):2036-42. Epub 20170511. doi: 10.1016/j.bbamcr.2017.05.010. PubMed PMID: 28502592.
76. Hautz T, Salcher S, Fodor M, Sturm G, Ebner S, Mair A, et al. Immune cell dynamics deconvoluted by single-cell RNA sequencing in normothermic machine perfusion of the liver. Nat Commun. 2023;14(1):2285. Epub 2023/04/22. doi: 10.1038/s41467-023-37674-8. PubMed PMID: 37085477; PubMed Central PMCID: PMCPMC10121614.
77. Browaeys R, Saelens W, Saeys Y. NicheNet: modeling intercellular communication by linking ligands to target genes. Nat Methods. 2020;17(2):159-62. Epub 2019/12/11. doi: 10.1038/s41592-019-0667-5. PubMed PMID: 31819264.
78. Perrault DP, Bramos A, Xu X, Shi S, Wong AK. Local Administration of Interleukin-1 Receptor Antagonist Improves Diabetic Wound Healing. Ann Plast Surg. 2018;80(5S Suppl 5):S317-S21. doi: 10.1097/SAP.0000000000001417. PubMed PMID: 29553981; PubMed Central PMCID: PMCPMC5929157.
79. Cong L, Maishi N, Annan DA, Young MF, Morimoto H, Morimoto M, et al. Inhibition of stromal biglycan promotes normalization of the tumor microenvironment and enhances chemotherapeutic efficacy. Breast Cancer Res. 2021;23(1):51. Epub 20210510. doi: 10.1186/s13058-021-01423-w. PubMed PMID: 33966638; PubMed Central PMCID: PMCPMC8108358.
80. Morimoto H, Hida Y, Maishi N, Nishihara H, Hatanaka Y, Li C, et al. Biglycan, tumor endothelial cell secreting proteoglycan, as possible biomarker for lung cancer. Thorac Cancer. 2021;12(9):1347-57. Epub 20210311. doi: 10.1111/1759-7714.13907. PubMed PMID: 33709550; PubMed Central PMCID: PMCPMC8088962.

81. Dauphinee SM, Karsan A. Lipopolysaccharide signaling in endothelial cells. Lab Invest. 2006;86(1):9-22. doi: 10.1038/labinvest.3700366. PubMed PMID: 16357866.
82. Lloyd KL, Kubes P. GPI-linked endothelial CD14 contributes to the detection of LPS. Am J Physiol Heart Circ Physiol. 2006;291(1):H473-81. Epub 20060127. doi: 10.1152/ajpheart.01234.2005. PubMed PMID: 16443672.
83. Wilkinson HN, Hardman MJ. Wound healing: cellular mechanisms and pathological outcomes. Open Biol. 2020;10(9):200223. Epub 20200930. doi: 10.1098/rsob.200223. PubMed PMID: 32993416; PubMed Central PMCID: PMCPMC7536089.
84. Du Cheyne C, Tay H, De Spiegelaere W. The complex TIE between macrophages and angiogenesis. Anat Histol Embryol. 2020;49(5):585-96. Epub 20191127. doi: 10.1111/ahe.12518. PubMed PMID: 31774212.
85. Pakyari M, Farrokhi A, Maharlooei MK, Ghahary A. Critical Role of Transforming Growth Factor Beta in Different Phases of Wound Healing. Adv Wound Care (New Rochelle). 2013;2(5):215-24. doi: 10.1089/wound.2012.0406. PubMed PMID: 24527344; PubMed Central PMCID: PMCPMC3857353.
86. Cutroneo KR. TGF-beta-induced fibrosis and SMAD signaling: oligo decoys as natural therapeutics for inhibition of tissue fibrosis and scarring. Wound Repair Regen. 2007;15 Suppl 1:S54-60. doi: 10.1111/j.1524-475X.2007.00226.x. PubMed PMID: 17727468.
87. Krzyszczyk P, Schloss R, Palmer A, Berthiaume F. The Role of Macrophages in Acute and Chronic Wound Healing and Interventions to Promote Pro-wound Healing Phenotypes. Front Physiol. 2018;9:419. Epub 20180501. doi: 10.3389/fphys.2018.00419. PubMed PMID: 29765329; PubMed Central PMCID: PMCPMC5938667.
88. Kim SY, Nair MG. Macrophages in wound healing: activation and plasticity. Immunol Cell Biol. 2019;97(3):258-67. Epub 20190211. doi: 10.1111/imcb.12236. PubMed PMID: 30746824; PubMed Central PMCID: PMCPMC6426672.
89. Na YR, Yoon YN, Son DI, Seok SH. Cyclooxygenase-2 inhibition blocks M2 macrophage differentiation and suppresses metastasis in murine breast cancer model. PLoS One. 2013;8(5):e63451. Epub 20130507. doi: 10.1371/journal.pone.0063451. PubMed PMID: 23667623; PubMed Central PMCID: PMCPMC3646746.
90. Wang M, Chaudhuri R, Ong WWS, Sintim HO. c-di-GMP Induces COX-2 Expression in Macrophages in a STING-Independent Manner. ACS Chem Biol. 2021;16(9):1663-70. Epub 20210903. doi: 10.1021/acschembio.1c00342. PubMed PMID: 34478263.
91. Orecchioni M, Ghosheh Y, Pramod AB, Ley K. Macrophage Polarization: Different Gene Signatures in M1(LPS+) vs. Classically and M2(LPS-) vs. Alternatively Activated Macrophages. Front Immunol. 2019;10:1084. Epub 20190524. doi: 10.3389/fimmu.2019.01084. PubMed PMID: 31178859; PubMed Central PMCID: PMCPMC6543837.
92. Watanabe S, Alexander M, Misharin AV, Budinger GRS. The role of macrophages in the resolution of inflammation. J Clin Invest. 2019;129(7):2619-28. Epub 20190520. doi: 10.1172/JCI124615. PubMed PMID: 31107246; PubMed Central PMCID: PMCPMC6597225.
93. Girbl T, Lenn T, Perez L, Rolas L, Barkaway A, Thiriot A, et al. Distinct Compartmentalization of the Chemokines CXCL1 and CXCL2 and the Atypical Receptor ACKR1 Determine Discrete Stages of Neutrophil Diapedesis. Immunity. 2018;49(6):1062-76 e6. Epub 2018/11/18. doi: 10.1016/j.immuni.2018.09.018. PubMed PMID: 30446388; PubMed Central PMCID: PMCPMC6303217.
94. Sawant KV, Sepuru KM, Lowry E, Penaranda B, Frevert CW, Garofalo RP, et al. Neutrophil recruitment by chemokines Cxcl1/KC and Cxcl2/MIP2: Role of Cxcr2 activation and glycosaminoglycan interactions. J Leukoc Biol. 2021;109(4):777-91. Epub 2020/09/04. doi: 10.1002/JLB.3A0820-207R. PubMed PMID: 32881070; PubMed Central PMCID: PMCPMC8296306.
95. Dunny GM, Brown BL, Clewell DB. Induced cell aggregation and mating in Streptococcus faecalis: evidence for a bacterial sex pheromone. Proc Natl Acad Sci U S A. 1978;75(7):3479-83. Epub 1978/07/01. doi: 10.1073/pnas.75.7.3479. PubMed PMID: 98769; PubMed Central PMCID: PMCPMC392801.
96. Ahlmann-Eltze C, Huber W. glmGamPoi: fitting Gamma-Poisson generalized linear models on single cell count data. Bioinformatics. 2021;36(24):5701-2. Epub 2020/12/10. doi: 10.1093/bioinformatics/btaa1009. PubMed PMID: 33295604; PubMed Central PMCID: PMCPMC8023675.
97. Germain PL, Lun A, Garcia Meixide C, Macnair W, Robinson MD. Doublet identification in single-cell sequencing data using scDblFinder. F1000Res. 2021;10:979. Epub 20210928. doi:

10.12688/f1000research.73600.2. PubMed PMID: 35814628; PubMed Central PMCID: PMCPMC9204188.
98. Choudhary S, Satija R. Comparison and evaluation of statistical error models for scRNA-seq. Genome Biol. 2022;23(1):27. Epub 2022/01/20. doi: 10.1186/s13059-021-02584-9. PubMed PMID: 35042561; PubMed Central PMCID: PMCPMC8764781.
99. Bergen V, Lange M, Peidli S, Wolf FA, Theis FJ. Generalizing RNA velocity to transient cell states through dynamical modeling. Nat Biotechnol. 2020;38(12):1408-14. Epub 2020/08/05. doi: 10.1038/s41587-020-0591-3. PubMed PMID: 32747759.
100. Hao Y, Hao S, Andersen-Nissen E, Mauck WM, 3rd, Zheng S, Butler A, et al. Integrated analysis of multimodal single-cell data. Cell. 2021;184(13):3573-87 e29. Epub 2021/06/02. doi: 10.1016/j.cell.2021.04.048. PubMed PMID: 34062119; PubMed Central PMCID: PMCPMC8238499.
101. McInnes L, Healy J, Melville J. Umap: Uniform manifold approximation and projection for dimension reduction. arXiv preprint arXiv:180203426. 2018.
102. Langfelder P, Horvath S. WGCNA: an R package for weighted correlation network analysis. BMC Bioinformatics. 2008;9:559. Epub 2008/12/31. doi: 10.1186/1471-2105-9-559. PubMed PMID: 19114008; PubMed Central PMCID: PMCPMC2631488.
103. Keogh D, Tay WH, Ho YY, Dale JL, Chen S, Umashankar S, et al. Enterococcal Metabolite Cues Facilitate Interspecies Niche Modulation and Polymicrobial Infection. Cell Host Microbe. 2016;20(4):493-503. doi: 10.1016/j.chom.2016.09.004. PubMed PMID: 27736645; PubMed Central PMCID: PMCPMC5076562.
104. Toda G, Yamauchi T, Kadowaki T, Ueki K. Preparation and culture of bone marrow-derived macrophages from mice for functional analysis. STAR Protoc. 2021;2(1):100246. Epub 2021/01/19. doi: 10.1016/j.xpro.2020.100246. PubMed PMID: 33458708; PubMed Central PMCID: PMCPMC7797923.
105. Pfaffl MW, Tichopad A, Prgomet C, Neuvians TP. Determination of stable housekeeping genes, differentially regulated target genes and sample integrity: BestKeeper--Excel-based tool using pair-wise correlations. Biotechnol Lett. 2004;26(6):509-15. Epub 2004/05/07. doi: 10.1023/b:bile.0000019559.84305.47. PubMed PMID: 15127793.
106. Roca CP, Burton OT, Neumann J, Tareen S, Whyte CE, Gergelits V, et al. A cross entropy test allows quantitative statistical comparison of t-SNE and UMAP representations. Cell Rep Methods. 2023;3(1):100390. Epub 20230113. doi: 10.1016/j.crmeth.2022.100390. PubMed PMID: 36814837; PubMed Central PMCID: PMCPMC9939422.
107. Ianevski A, Giri AK, Aittokallio T. Fully-automated and ultra-fast cell-type identification using specific marker combinations from single-cell transcriptomic data. Nat Commun. 2022;13(1):1246. Epub 20220310. doi: 10.1038/s41467-022-28803-w. PubMed PMID: 35273156; PubMed Central PMCID: PMCPMC8913782.

METHODS

KEY RESOURCES TABLE

REAGENT or RESOURCE	SOURCE	IDENTIFIER
Chemicals		
Bovine serum albumin	Merck	A7030
Brain Heart Infusion medium	Merck	53286
Collagenase type I	Thermo Fisher Scientific	17100017
Dispase II	Thermo Fisher Scientific	17105041
Dulbecco's phosphate buffered saline w/o Ca2+ and Mg2+	Thermo Fisher Scientific	141900094
Hank's balanced salt solution w/o Ca^{2+} and Mg^{2+}	Thermo Fisher Scientific	88284
Isoflurane	Vetpharma Animal Health	NA
Liberase TM	Merck	5401119001
Luna SYBR Green	New England Biolabs	M3003
Nair Moisturising Hair Removal Cream	Chruch and Dwight Co	NA
Recombinant Mouse M-CSF	BioLegend	576404
Phosphate buffered saline	Gibco	14190144
TRIzol	Invitrogen	15596018
Trypsin/EDTA	Gibco	25-051-CI
Chromium Next GEM Chip G Single Cell Kit	10x Genomics	1000127
Chromium Next GEM Single Cell 3' Gel Bead Kit v3.1	10x Genomics	1000129
Chromium Next GEM Single Cell 3' GEM Kit v3.1	10x Genomics	1000130
Chromium Next GEM Single Cell 3' Kit v3.1	10x Genomics	1000269
Critical Commercial Assays		
Dual Index Kit TT Set A	10x Genomics	1000215
EZ-10 DNAaway RNA Mini-Preps kit	Bio Basic	BS88136-250
Library Construction Kit	10x Genomics	1000196
RevertAid Reverse Transcriptase	Thermo Fisher	01327685
Tube, Dynabeads MyOne SILANE	10x Genomics	2000048
Bacterial Strains		
Enterococcus faecalis OG1RF	Dunny *et al*.[95]	WT OG1RF
Oligonucleotides		
Gene	Forward	Reverse
ActB	ATC AGC AAG CAG GAG TAC GAT	GTG TAA AAC GCA GCT CAG TAA CA

Arg1	CAG AAG AAT GGA AGA GTC AG	CAG ATA TGC AGG GAG TCA CC
Egf	TGG CTC GAA GTC AGA TCC ACA	TTC TCG GGC ACA TGG TTA ATG
Gapdh	TCA GGA GAG TGT TTC CTC GTC CC	TCT CGG CCT TGA CTG TGC CG
Fgf1	CCC TGA CCG AGA GGT TCA AC	GTC CCT TGT CCC ATC CAC G
Mrc1	TTC AGC TAT TGG ACG CGA GG	GAA TCT GAC ACC CAG CGG AA
Nos2	TGT CGC AGC TCC CTA TCT TG	GGA AGC CAC TGA CAC TTC GC
Pdgfa	TGG CTC GAA GTC AGA TCC ACA	TTC TCG GGC ACA TGG TTA ATG
Tgfb1	GGA AAT CAA CGG GAT CAG CCC	GCT GCC GCA CAC AGC AGT TC
Ubc	CCC AGT GTT ACC ACC AAG AAG	CCC CAT CAC ACC CAA GAA CA
Deposited Data		
Raw and processed scRNA-seq data	NCBI Gene Expression Omnibus	GSE229257
Processed Seurat Object	Zenodo	https://doi.org/10.5281/zenodo.7608212
Experiment Models: Organisms/Strain		
Mouse C57BL/6	InVivos	n/a
Software and Algorithms		
anndata 0.8.0	PyPI	https://pypi.org
BioRender	https://biorender.com	n/a
CellChat 1.6.1	Jin *et al*.[35]	Jin *et al*.[35]
cellrank 1.5.1	Lange *et al*.[45]	Lange *et al*.[45]
Cell Ranger 6.1.2	10X Genomics, Inc.	https://www.10xgenomics.com
clustree 0.5.0	Zappia *et al*.[40]	Zappia *et al*.[40]
glmGamPoi 1.8.0	Ahlmann-Eltze *et al*.[96]	Ahlmann-Eltze *et al*.[96]
miQC 1.4.0	GitHub	https://github.com/greenelab/miQC
NicheNet	Browaeys *et al*.[77]	Browaeys *et al*.[77]
numpy 1.23.5	PyPI	https://pypi.org
pandas 1.5.3	PyPI	https://pypi.org
PanglaoDB	PanglaoDB	https://panglaodb.se/markers.html
Prism 9.4.1	GraphPad Software	https://www.graphpad.com
PyCharm 2022.3.3	JetBrains	https://www.jetbrains.com
Python 3.9.16	Python Software Foundation	https://python.org
R 4.2.1	The R Foundation	https://www.r-project.org
RStudio 2022.07.2+576	Posit Software	https://posit.co
samtools 1.13	GitHub	https://github.com/samtools
scanpy 1.9.1	PyPI	https://pypi.org
scipy 1.10.0	PyPI	https://pypi.org
scDblFinder 1.10.0	Germain *et al*.[97]	Germain *et al*.[97]
sctransform 0.3.5	Choudhary *et al*.[98]	Choudhary *et al*.[98]

scvelo 0.2.5	Bergen *et al*.[99]	Bergen *et al*.[99]
Seurat 4.3.0	Hao *et al*.[100]	Hao *et al*.[100]
UMAP	McInnes *et al*.[101]	https://github.com/lmcinnes/umap
velocyto.py 0.17.17	La Manno *et al*.[44]	La Manno *et al*.[44]
WGCNA 1.72-1	Langfelder *et al*.[102]	Langfelder *et al*.[102]

RESOURCE AVAILABILITY

Lead Contact

Further information and requests for resources should be directed to and will be fulfilled by the lead contacts, Kimberly Kline, at kimberly.kline@unige.ch and Guillaume Thibault, at thibault@ntu.edu.sg.

Material Availability

This study did not generate new reagents.

Data and Code Availability

The accession number for the raw data reported in this paper is GSE229257. The processed data are available at Zenodo (https://doi.org/10.5281/zenodo.7608212).

METHOD DETAILS

Mouse wound infection model

In vivo procedures were approved by the Animal Care and Use Committee of the Biological Resource Centre (Nanyang Technological University, Singapore) in accordance with the guidelines of the Agri-Food and Veterinary Authority and the National Advisory Committee for Laboratory Animal Research of Singapore (ARF SBS/NIEA-0314). Male C57BL/6 mice were housed at the Research Support Building animal facility under pathogen-free conditions. Mice between 5-7 weeks old (22–25 g; InVivos, Singapore) were used for the wound infection model, modified from a previous study[103]. Briefly, mice were anesthetized with 3% isoflurane. Dorsal hair was removed by shaving, followed by hair removal cream (Nair cream, Church and Dwight Co) application. The shaven skin was then disinfected with 70% ethanol and a 6-mm full-thickness wound was created using a biopsy punch (Integra Miltex, New York). Two mice were infected with 10 µl of 2 x10^8 bacteria/ml inoculum (*Enterococcus faecalis* OG1RF strain), while the other two served as controls for uninfected wounds. All wounds were sealed with

transparent dressing (Tegaderm, 3M, St Paul Minnesota). Mice were euthanized four days post-infection (4 dpi), and wounds collected immediately using a biopsy punch with minimal adjacent healthy skin were stored in Hanks 'Buffered Salt Solution (HBSS; Ca^{2+}/Mg^{2+}-free; Sigma Aldrich, Cat. #H4385) supplemented with 0.5% bovine serum albumin (BSA; Sigma Aldrich, Cat. #A7030).

In vitro culture and infection of bone marrow-derived macrophages

Murine bone marrow-derived macrophages (BMDMs) were isolated from bone marrow cells of 7-8 weeks old C57BL/6 male mice as described previously[104], except that BMDMs were differentiated in 100 mm non-treated square dishes (Thermo Scientific, Singapore) with supplementation of 50 ng/ml M-CSF (BioLegend, Singapore). On day 6, differentiated BMDMs were harvested by gentle cell scraping in Dulbecco's PBS (DPBS; Gibco, Singapore), and 10^6 BMDMs were seeded in 6-well plates using bone marrow growth medium without antibiotics. Following overnight incubation, the growth medium was replaced with complete DMEM (DMEM supplemented with 10% FBS) for *E. faecalis* infection. Log-phase *E. faecalis* OG1RF cultures were washed and normalized to an OD_{600}/ml of 0.5 in complete DMEM, equivalent to approximately 3 x 10^8 CFU/ml. BMDMs were then infected with OG1RF at a multiplicity of infection (MOI) of 10 for 1 h, followed by centrifugation at 1,000 x *g* for 5 min prior to incubation to promote BMDM-bacteria contact. For uninfected controls, complete DMEM was added instead of MOI 10 bacterial suspension. At 1 hpi, BMDM were washed thrice with DPBS and incubated in complete DMEM supplemented with 10 µg/ml vancomycin and 150 µg/ml gentamicin for 23 h to kill extracellular bacteria, until a final time point of 24 hpi.

Quantitative qPCR analysis

Total mRNA was extracted using the TRIzol reagent (Invitrogen, cat. # 15596018) and purified using an EZ-10 DNAaway RNA Mini-Preps Kit (Bio Basic, cat. #BS88136-250). Complementary DNA (cDNA) was synthesized from total RNA using RevertAid Reverse Transcriptase (Thermo Fisher, Waltham, MA, cat. # 01327685) according to the manufacturer's protocol. Real-time PCR was performed using Luna SYBR Green (New England Biolabs, UK) according to the manufacturer's protocol using a CFX-96 Real-time PCR system (Bio-Rad, Hercules, CA, USA). A 100-ng of cDNA and 0.25 µM of the paired primer mix for target genes were used for each reaction. Relative mRNA was normalized to the housekeeping gene glyceraldehyde-3-phosphate dehydrogenase (*Gapdh*) or a geometric mean of Ct

values from beta-actin (*Actb*) and ubiquitin (*Ubc*) housekeeping genes, as calculated by BestKeeper[105] and log2 fold changes were plotted with reference to the uninfected, unwounded skin. The primer pairs used in this study are listed in the Key Resources Table.

Dissociation of tissue and library preparation

Tissues were transferred to a sterile 10 mm^2 tissue culture dish and cut into small fragments using a sterile blade. The dissociation cocktail [10 mg/ml of dispase II (GIBCO, Cat. #17105041), 250 mg/ml of collagenase type I (GIBCO, cat. #17100017), and 2.5 mg/ml of liberase TM (Roche, cat. #5401119001)] was dissolved in HBSS. The tissue was digested enzymatically in pre-warmed dissociation buffer for 2 h at 37°C with manual orbital shaking every 15 min and then the dissociated cells were sifted through a sterile 70-µm cell strainer (Corning, cat. #352350) on ice and washed thrice with HBSS supplemented with 0.04% BSA. The remaining undigested tissue on the filter was re-incubated in 0.05%$^{w/v}$ trypsin/EDTA (GIBCO, cat. #25-051-CI) for 15 min at 37°C. Trypsin-digested cells were pooled with cells on ice by sifting through a sterile 70-µm cell strainer. The pooled cell suspension was washed thrice with HBSS supplemented with 0.04% BSA, followed by final filtering using a sterile 40-µm cell strainer (Corning, cat. #352340). The cell suspensions were centrifuged at 300 x *g* for 10 min, and the pellets were resuspended in Dulbecco's phosphate-buffered saline (DPBS; Thermo Fisher Scientific, cat. #14190094). Cell viability was determined by using Countess 3 FL Automated Cell Counter (Invitrogen) by mixing cell suspension with 0.4% trypan blue stain (Invitrogen, cat. #T10282) at a ratio of 1:1 for a minimum of four counts per sample. Isolated cells were encapsulated for single-cell RNA sequencing with microfluidic partitioning using the Chromium Single Cell 3' Reagent Kits (v3.1 Chemistry Dual Index, Protocol #CG000315), targeting 8,000 cells (10X Genomics, Pleasanton, CA). Libraries then were pooled by condition and sequenced on the HiSeq6000 system by NovogeneAIT (Singapore). A detailed protocol can be found at protocols.io (dx.doi.org/10.17504/protocols.io.yxmvmn8m9g3p/v1).

Data Processing

Raw data (.bcl) was used as an input to *Cell Ranger* (v6.1.2, 10X Genomics) with `mkfastq` function for trimming, base calling, and demultiplexing of reads by NovogeneAIT (Singapore). FASTQ files were aligned, filtered, barcoded and UMI counted using `cellranger count` command using *GENCODE*

vM23/Ensembl 98 (https://cf.10xgenomics.com/supp/cell-exp/refdata-gex-GRCh38-2020-A.tar.gz) mouse reference genome with `--expect cells` of 8,000 per sample on the National Supercomputer Centre Singapore (NSCC) High Power Computing platform (ASPIRE 1). The raw data can be found at Gene Expression Omnibus with the accession number GSE229257.

Integration and downstream analysis

Datasets from each sample were integrated using *Seurat* version 4.3.0[100] on *R* (v4.2.1) using *RStudio* interface (RStudio 2022.07.2+576 "Spotted Wakerobin" release) on macOS Ventura (13.0.1). Briefly, Seurat objects were created based on the criteria of a minimum of 3 cells expressing a minimum of 200 features. Low-quality cells were determined by a probabilistic approach using the *miQC* package (v1.4.0). Similarly, doublets were removed with *scDblFinder* v1.10.0[97]. Cell cycle stages were determined by using *Seurat*'s built-in updated cell-cycle gene list. Feature counts were normalized using `SCTransform()` v2 regularization[98] with a scaling factor of $1x10^4$ and Gamma-Poisson Generalized Linear Model by `glmGamPoi()` function[96], during which cell cycles and mitochondrial genes were regressed out for integration of 3,000 anchors. Fourteen principal components (PC) were included in dimension reduction calculated by the point where the change of percentage of variation was more than 0.1% between the two consecutive PCs. First, *k*-Nearest Neighbors were computed using *pca* reduction, followed by identifying original Louvain clusters with a resolution of 0.7 calculated by *clustree* v0.5.0[40]. Uniform Manifold Approximation and Projection (UMAP) was used for visualization throughout the study[101]. A log 2-fold-change of 0.5 was set to identify gene expression markers for all clusters with `min.pct` of 0.25. Density plots were generated in the *Nebulosa* (v1.6.0) package to demonstrate specific cell population signatures. Finally, we computed weighted gene co-expression networks for describing the correlation patterns among genes across samples[102]. We also compared the 2D UMAP representations of the two conditions. Using the integrated dataset, we split the dataset based on the conditions by the built-in `SplitObject()` function of the Seurat package. Then, we computed a cross-entropy test for the UMAP projections by applying a two-sided Kolmogorov-Smirnov test[106].

Cell type annotation

An unbiased cell annotation was conducted at two levels using the *ScType* algorithm with slight modifications[107]. First, we identified mega classes using gene set signatures on PanglaoDB (https://panglaodb.se/; Acc. date August 2022). Secondly, we further detailed each cluster based on published comprehensive mouse skin datasets[3, 5]. The processed Seurat object can be found at Zenodo (https://doi.org/10.5281/zenodo.7608212).

Cell-cell interactions

NicheNet's differential *R* implementation (v1.1.1) was used to interrogate cell-cell interactions[77]. Three databases provided, namely *ligand-target prior model*, *ligand-receptor network*, and *weighted integrated networks*, were used *NicheNet*'s *Seurat* wrapper where endothelial cells were set as the receiver (receptor) cell population, and keratinocytes, fibroblasts, and macrophages were defined as the sender (ligand) populations. The *NicheNet* heat map was plotted to visualize the ligand activity-target cell gene expression matrix. We further compared cell-cell interactions between different niches to better predict niche-specific ligand-receptor (L-R) pairs using differential *NicheNet* analysis. *CellChat* (v1.6.1) was used to further identify secreted ligand-receptor pairs across all cell populations[35].

RNA velocity analysis

BAM files generated during the alignment of the raw data in Cell Ranger, were sorted by cell barcodes with `sort -t CB` using *samtools* (v1.13) in the command line. Spliced and unspliced reads were annotated in *velocyto.py* (v0.17.17) pipeline[44], with repeats mask annotation file downloaded from https://genome.ucsc.edu/ for mouse reference genome to generate `.loom` files. To solve full transcriptomics dynamics, we used the generalized dynamic model on *scVelo* v0.2.0[99] in *Python* 3 (v3.9.16) virtual environment set up in PyCharm (Education License v2022.3.3, build PY-223.8836.43; JetBrains, Czechia), and visualized main cell populations and subset analysis with velocity stream plots and individual genes that drive RNA velocity. Lineage driving genes were computed in *CellRank* v1.5.1[45]. Annotated data (`anndata`) files for each cell population and condition can be found at https://doi.org/10.5281/zenodo.7608772. The R scripts and complete *Jupyter* notebooks are also available at https://github.com/cenk-celik/Celik_et_al.

Statistical analysis

Statistical analyses were performed in *R*, python and Prism 9 (v9.4.1, GraphPad) whichever was applicable for the type of analysis. *P* values were adjusted with the Benjamini-Hochberg method for high-dimensional data analysis. The details of the significance and type of the test were indicated in the figure legends. Data are expressed as median ± SEM. A p-value of 0.05 was set as a significance threshold unless stated otherwise.

FIGURE LEGENDS

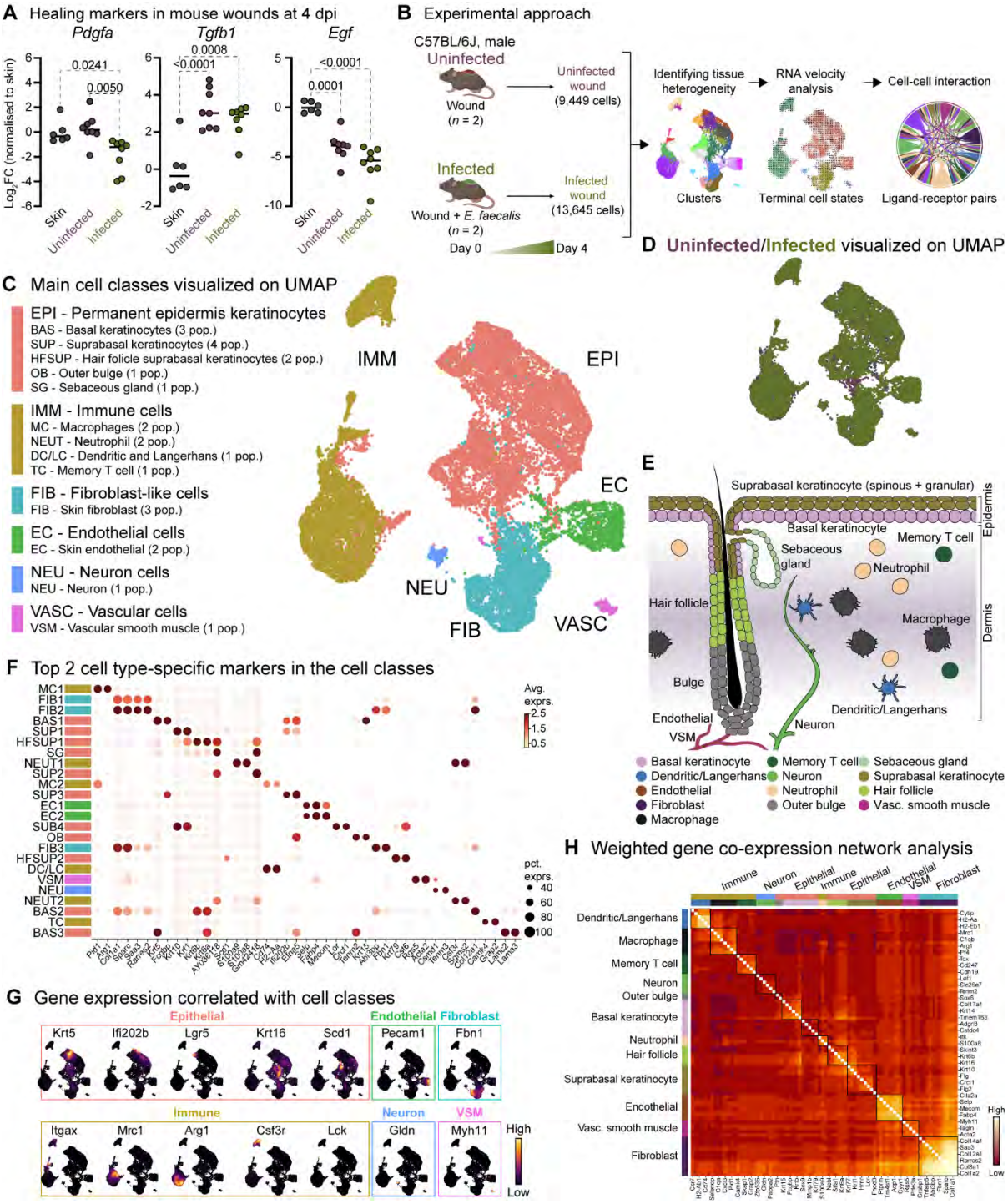

Figure 1. Mouse skin wound infection atlas.

(A) Gene expression of healing markers *Pdgfa*, *Tgfb1* and *Egf* four days post-infection (4 dpi) for uninfected and *E. faecalis*-infected 6–7-week-old C57BL/6J mouse skin wounds, normalized to intact skin (n = 6 for skin; n = 8 for wounds; one-way ANOVA). **(B)** Single-cell RNA sequencing workflow of

full-thickness mouse wounds. **(C)** Integrated dataset of ~23,000 scRNA-seq libraries from uninfected and infected wounds identifies 5 mega cell classes indicated in the UMAP. **(D)** UMAP colored by the uninfected and infected conditions. **(E)** Schematic describing the color-matched cell types with that of the clusters in Figure S1F. **(F)** Dot plot depicting the top two cell type-specific markers in the integrated data. Legend indicates average expression and dot size represents percent expression. **(G)** Density plots depict cell types described in C. **(H)** Heat map of weighted gene co-expression network analysis for annotated cell populations, colored by bars matching mega clusters and annotated cell types in C.

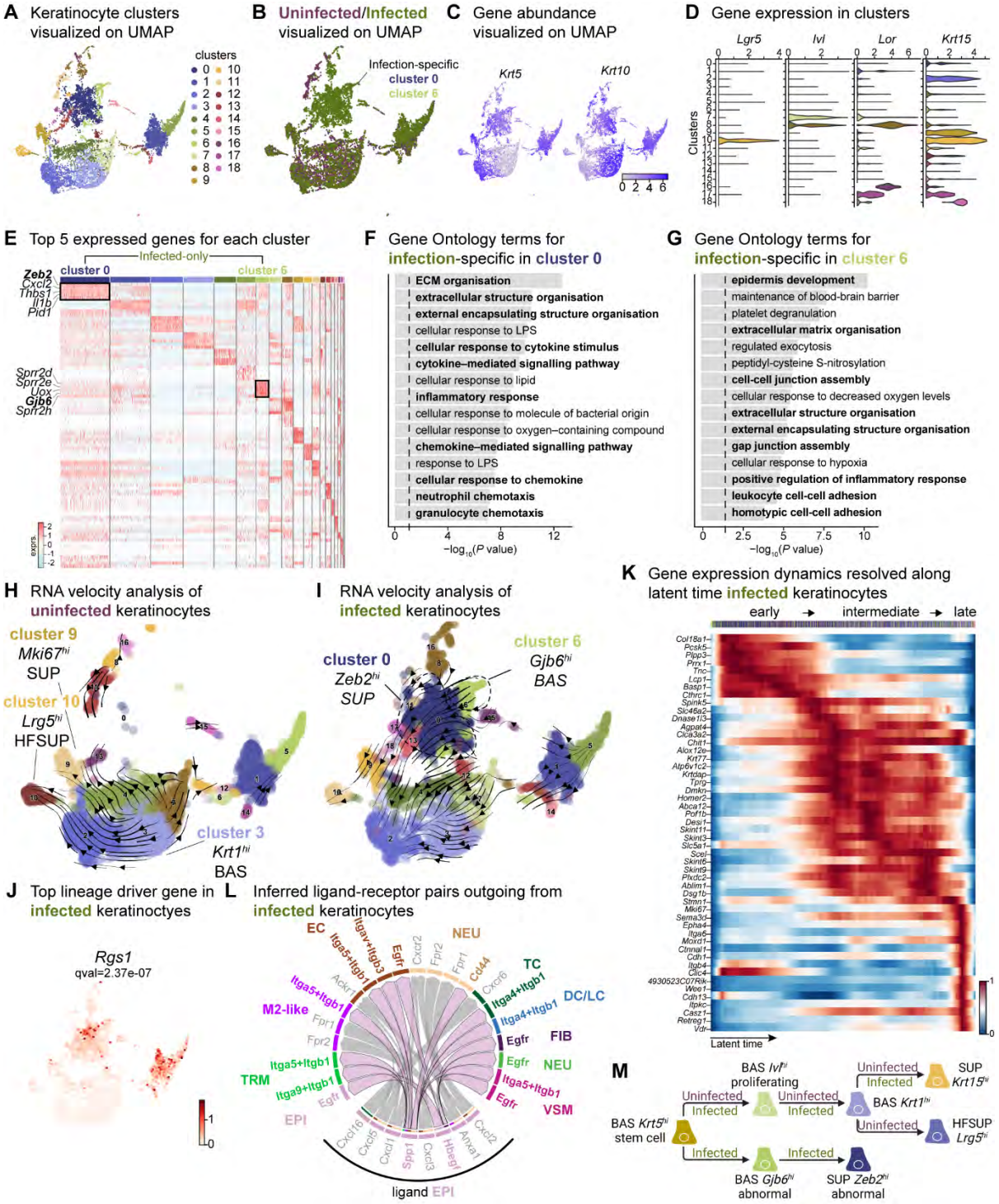

Figure 2. Sub-clustering of keratinocyte populations reveals infection-specific cell types.

(A) UMAP of integrated keratinocyte (basal, suprabasal, hair follicle, bulge, and sebaceous gland) population reveals 19 clusters. **(B)** Infected keratinocytes (green) show unique and shared clusters with uninfected keratinocytes (purple). **(C)** Spatial dispersion of *Krt5* and *Krt10* abundance in keratinocytes. **(D)** Expression of *Lgr5*, *Ivl*, *Lor*, and *Krt15* in Louvain clusters shown in A. **(E)** Heat map of top 5 differentially expressed marker genes for each cluster in keratinocytes. Rectangle boxes indicate

infection-specific Louvain clusters. **(F-G)** The bar plots show the top 15 Gene Ontology terms for infection-specific (F) *Zeb2*^{hi} (cluster 0) and (G) *Gjb6*^{hi} (cluster 6) keratinocyte populations. **(H-I)** Dynamic RNA velocity estimation of uninfected (H) and infected (I) keratinocytes. **(J)** The top lineage driver gene, *Rgs1*, in infected keratinocytes, was ubiquitously expressed in infection-specific Louvain clusters. (K) Gene expression dynamics resolved along latent time in the top 50 likelihood-ranked genes of infected keratinocytes. The colored bar at the top indicates Louvain clusters in I. Legend describes scaled gene expression. (L) Inferred ligand-receptor pairs outgoing from infected keratinocytes. (M) The hierarchy tree depicts the trajectory of differentiating and terminally differentiated keratinocyte cells originating from basal keratinocytes.

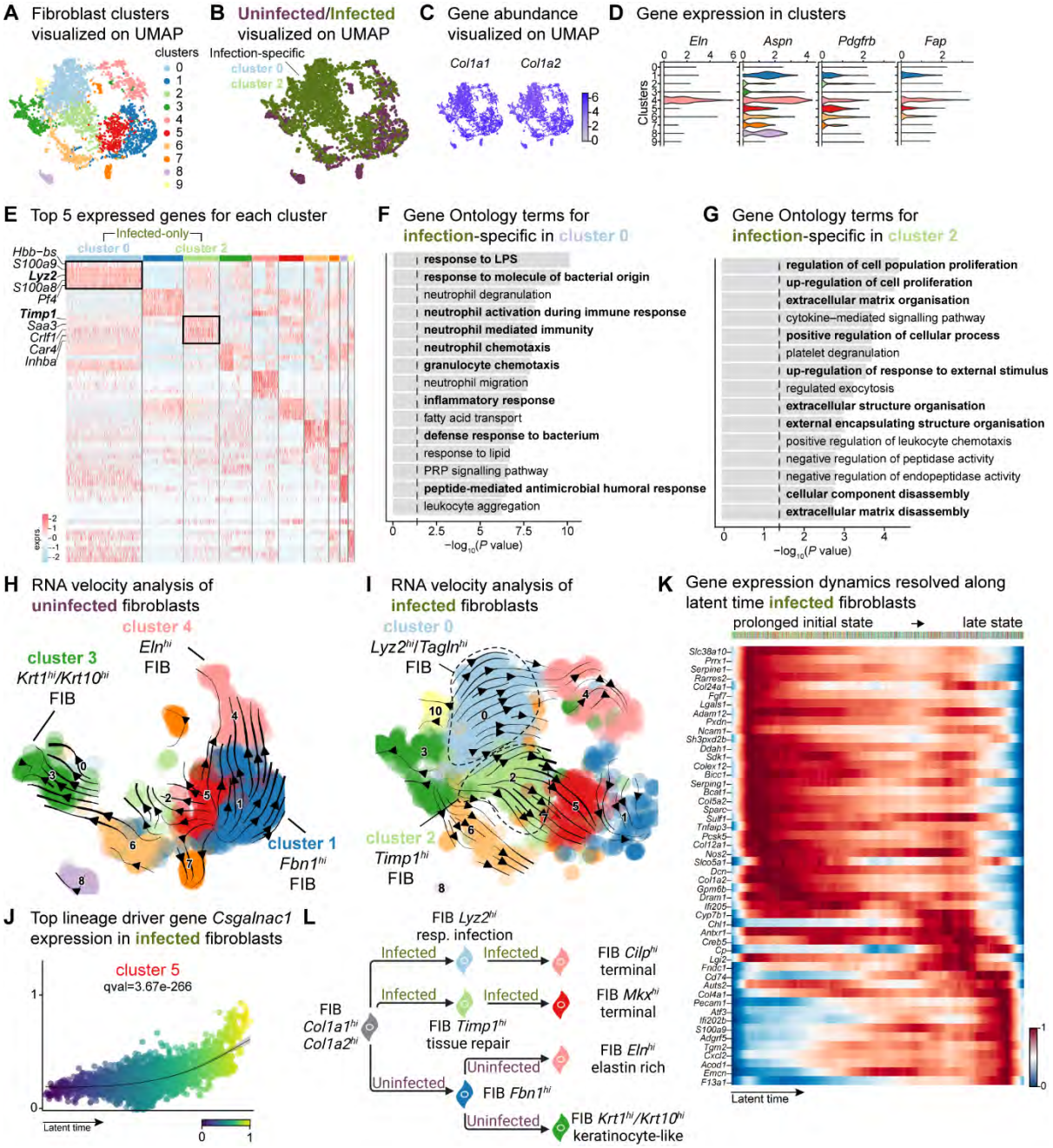

Figure 3. *E. faecalis* delays immune response in fibroblasts.

(A) UMAP of integrated fibroblasts reveals 12 clusters. **(B)** Infected fibroblasts (green) show unique and shared clusters with uninfected fibroblasts (purple). **(C)** Spatial dispersion of *Col1a1* and *Col1a2* abundance in fibroblasts. **(D)** Expression of *Eln*, *Aspn*, *Pdgfrb* and *Fap* in Louvain clusters shown in A. **(E)** Heat map of top 5 differentially expressed marker genes for each cluster in fibroblasts. Rectangle boxes indicate infection-specific Louvain clusters. **(F-G)** The bar plots show the top 15 Gene Ontology terms for infection-specific (F) *Lyz2*^{hi}/*Tagln*^{hi} (cluster 0) and (G) *Timp1*^{hi} (cluster 2) fibroblast populations. **(H-I)** Dynamic RNA velocity estimation of uninfected (H) and infected (I) fibroblasts. **(J)**

The top lineage driver gene, *Csgalnac1*, expression in infected fibroblasts. **(K)** Gene expression dynamics resolved along latent time in the top 50 likelihood-ranked genes of infected fibroblasts. The colored bar at the top indicates Louvain clusters in I. Legend describes scaled gene expression. **(L)** While uninfected fibroblasts show healing phenotypes, infected fibroblasts undergo two transitioning phases: (i) contractile and (ii) pathologic.

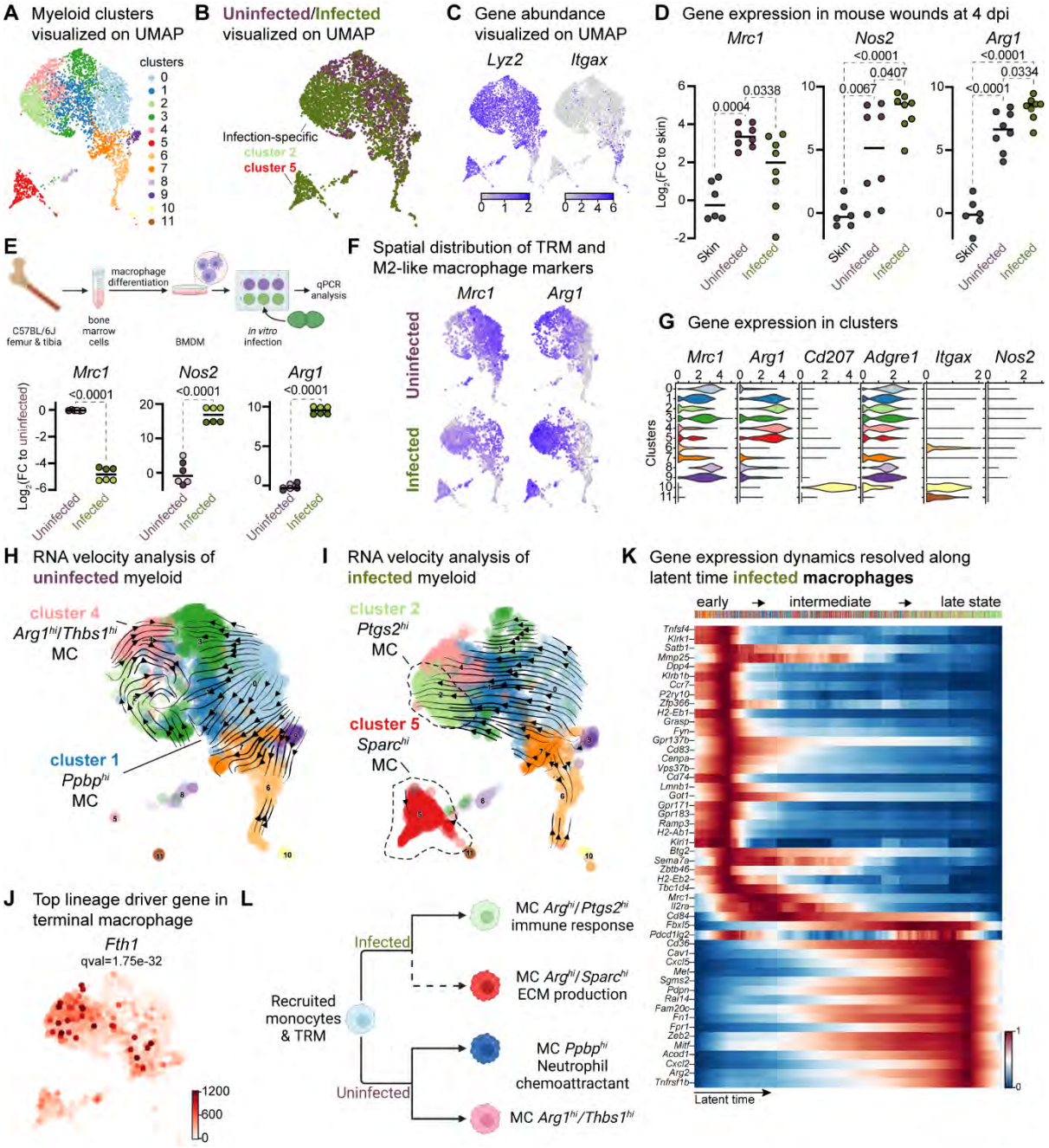

Figure 4. Macrophages display M2-like polarization.

(A) UMAP of the integrated myeloid population reveals 9 macrophages, 2 dendritic cells, and one Langerhans cell cluster. **(B)** Infected myeloid (green) population show unique and shared clusters with the uninfected myeloid (purple) population. **(C)** Spatial distribution of *Lyz2* (macrophage) and *Itgax* (DC and LC) abundance in fibroblasts. **(D)** Gene expression *Mrc1*, *Nos2* and *Arg1* in mouse wounds at 4dpi, normalized to homeostatic skin (n = 6 for skin; n = 8 for wounds; one-way ANOVA). **(E)** *In vitro* infection of unpolarized (M0) bone marrow-derived murine macrophages (BMDMs) resulted in a down-regulation of TRM-associated marker *Mrc1* and an upregulation of M2-like markers *Nos2* and *Arg1*. Data are

pooled from 2 biological replicates (shown in light and dark circles respectively) of 3 technical replicates each. **(F)** Spatial distribution of TRM and M2-like macrophage markers, *Mrc1* and *Arg1*, respectively. **(G)** Expression of *Mrc1*, *Adgre1*, *Arg1, Itgax*, *Cd207* and *Nos2* in the integrated myeloid dataset. **(H-I)** Dynamic RNA velocity estimation of uninfected (H) and infected (I) myeloid cells. **(J)** The top lineage driver gene, *Fth1*, was ubiquitously expressed in terminal macrophage populations. **(K)** Putative driver genes of infected macrophages. **(L)** The proposed model describes macrophage characteristics, where neutrophil-attracting and wound repair-associated macrophages were involved in uninfected wound healing. In contrast, bacteria-infected wounds are enriched in efferocytotic macrophages and matrix-producing macrophages.

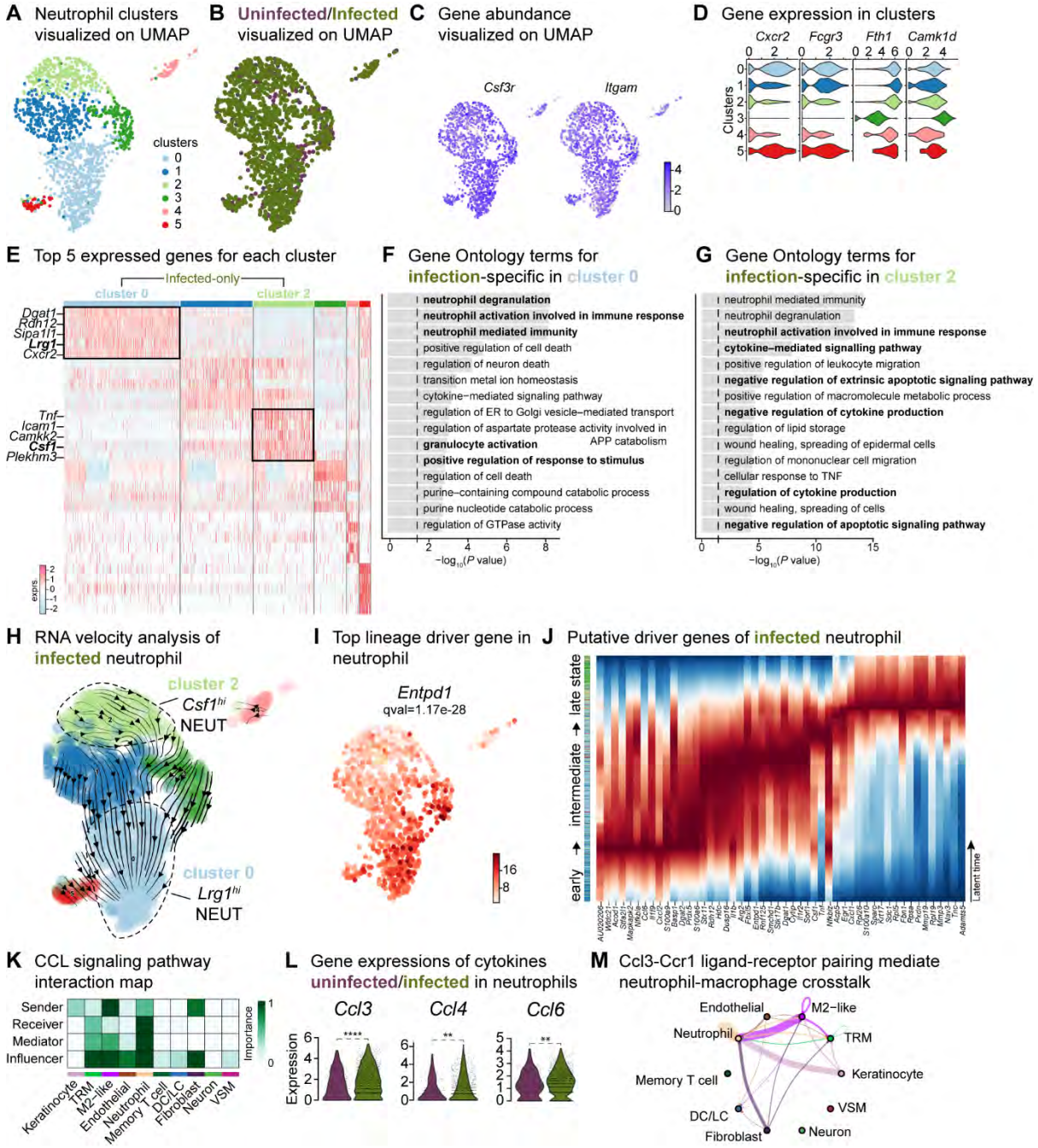

Figure 5. Crosstalk between neutrophils and anti-inflammatory macrophages regulates the CCL signaling pathway.

(A) UMAP of the integrated myeloid population reveals 6 Louvain clusters. **(B)** The infected neutrophil (green) population shows unique and shared clusters with the uninfected neutrophil (purple) population. **(C)** Spatial organization of *Csf3r* and *Itgam* abundance in neutrophils. **(D)** Expression of *Cxcr2*, *Fcgr3*, *Fth1* and *Camk1d* in Louvain clusters. **(E)** Heat map of top 5 differentially expressed marker genes in neutrophils. Rectangle boxes indicate infection-specific Louvain clusters. **(F-G)** The bar plots show the top 15 Gene Ontology terms for infection-specific (F) *Lrg1*^{hi} (cluster 0) and **(G)** *Csf1*^{hi} (cluster 2)

populations. **(H)** Dynamic RNA velocity estimation of infected neutrophils. **(I)** The top lineage driver gene, *Entpd1*, was ubiquitously expressed in *Lrg1*^{hi} neutrophils (cluster 0). **(J)** Putative driver genes of infected neutrophil clusters. **(K)** Cytokine signaling pathway (CCL) cell-cell interaction map. **(L)** Gene expression of cytokines *Ccl3*, *Ccl4,* and *Ccl6* in neutrophils. **(M)** Ccl3:Ccr1 ligand-receptor interaction mediate neutrophil-macrophage crosstalk.

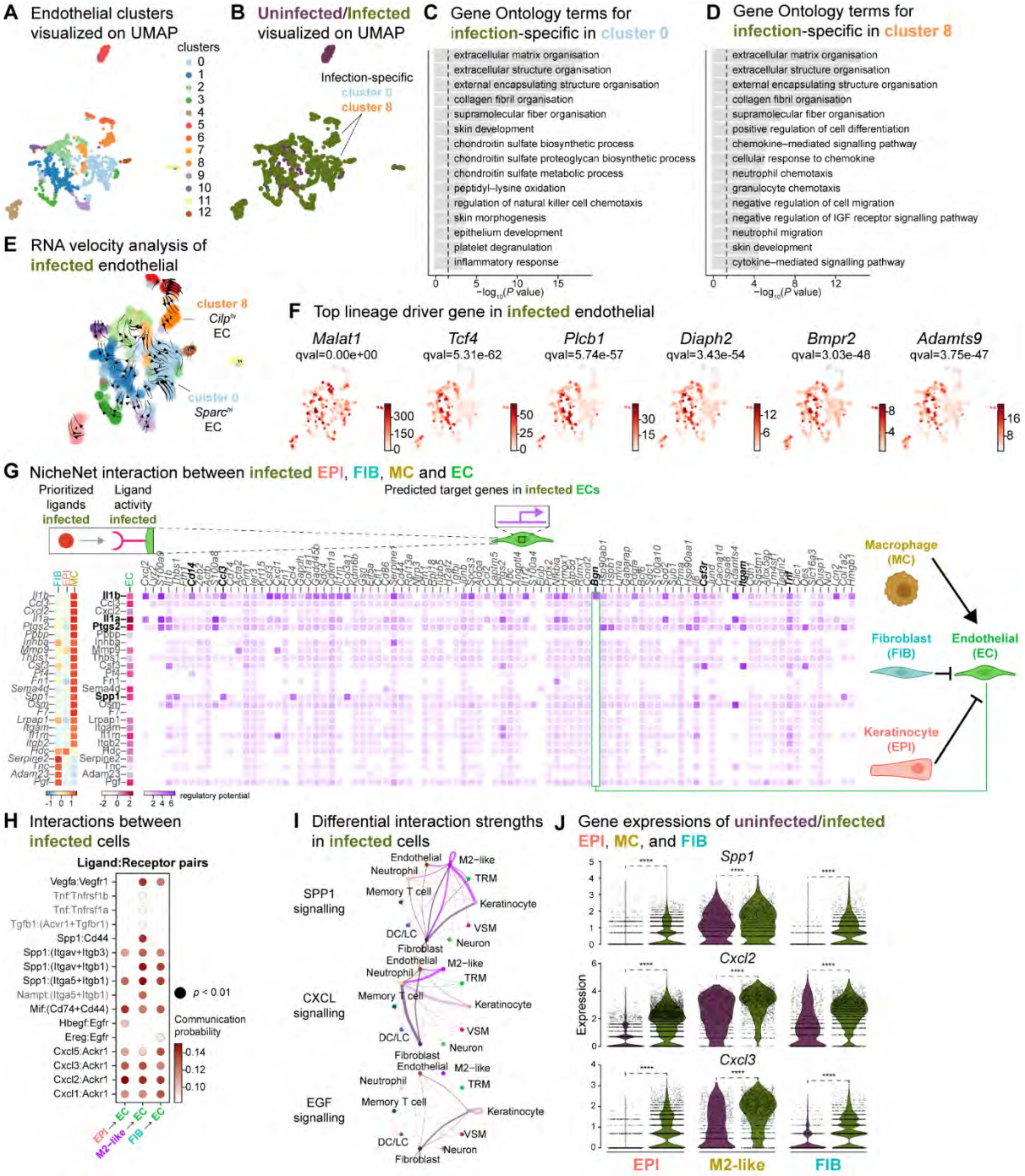

Figure 6. Macrophage-EC interactions display an anti-inflammatory niche.

(A) UMAP of integrated endothelial cells reveals 13 clusters. **(B)** Infected endothelial cells (green) show unique and shared clusters with uninfected endothelial cells (purple). **(C-D)** Gene Ontology analysis of infection-specific clusters 0 (C) and 8 (D). **(E)** Dynamic RNA velocity estimation of infected endothelial cells. **(F)** The top lineage driver genes, *Malat1*, *Tcf4, Plcb1, Diaph2, Bmpr2,* and *Adamts9* in infected endothelial cells. **(G)** NicheNet interaction heat map between keratinocytes, fibroblasts, macrophages, and endothelial cells. Note the macrophage *Il1b*-specific *Bgn* induction in infected ECs. **(H)** The dot plot

depicts interactions between endothelial cells (receptors) and keratinocytes, fibroblasts, and macrophages (ligands). Rows demonstrate a ligand-receptor pair for the indicated cell-cell interactions (column). **(I)** Differential interaction strengths of a cellular interactome for TNF, SPP1 and CXCL signaling pathways between all cell types in infection. **(J)** Spp1, Cxcl2, and Cxcl3 gene expression in keratinocytes, M2-like macrophages, and fibroblasts (Wilcoxon Rank Sum test, ****$p < 0.0001$).

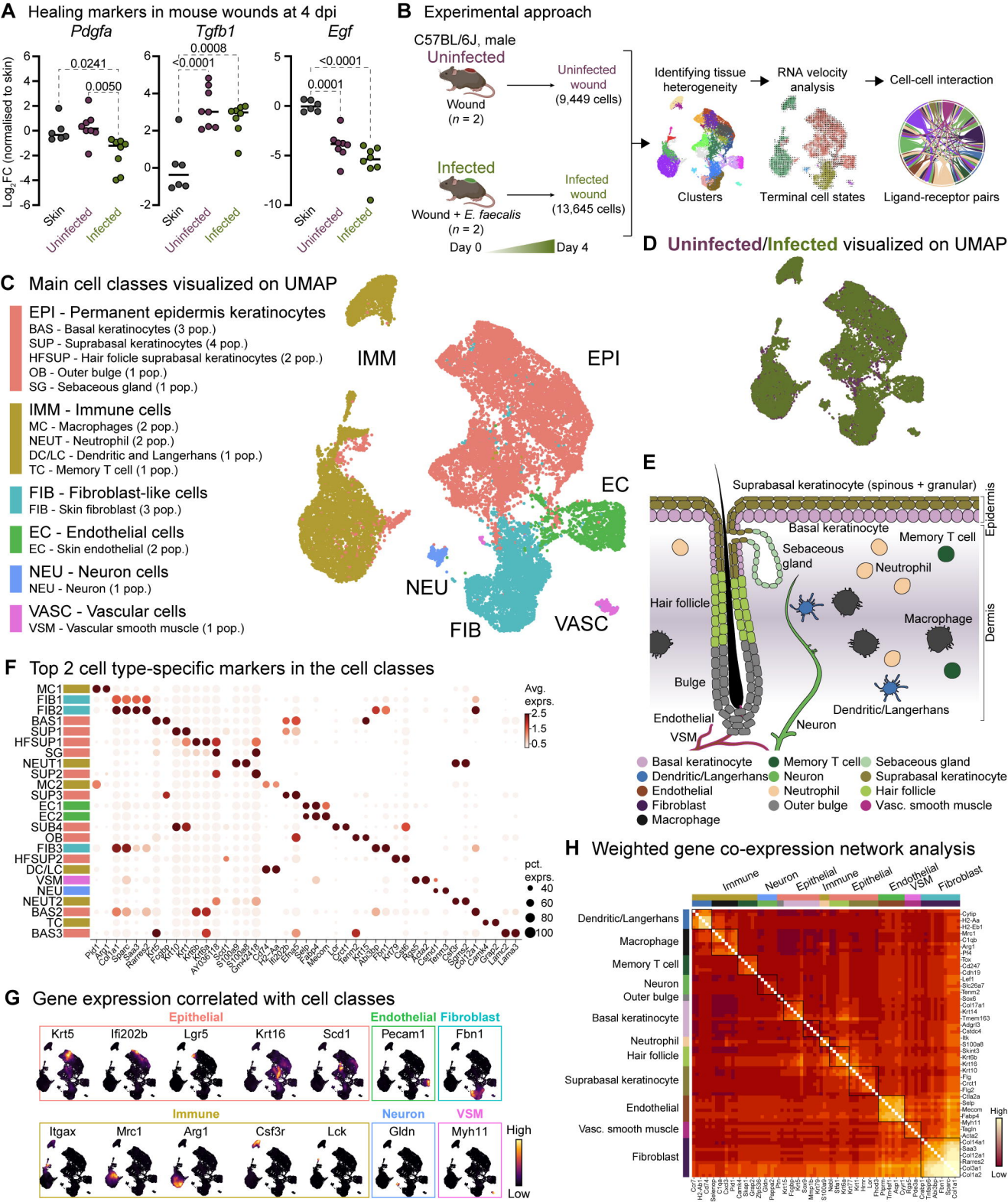
A Healing markers in mouse wounds at 4 dpi
Pdgfa
Tgfb1
Egf
Log2FC (normalised to skin)
0.0241
0.0050
0.0008
<0.0001
<0.0001
0.0001
Skin
Uninfected
Infected
B Experimental approach
C57BL/6J, male
Uninfected
Wound
(n = 2)
Uninfected wound
(9,449 cells)
Infected
Wound + E. faecalis
(n = 2)
Infected wound
(13,645 cells)
Day 0
Day 4
Identifying tissue heterogeneity
RNA velocity analysis
Cell-cell interaction
Clusters
Terminal cell states
Ligand-receptor pairs
C Main cell classes visualized on UMAP
EPI - Permanent epidermis keratinocytes
BAS - Basal keratinocytes (3 pop.)
SUP - Suprabasal keratinocytes (4 pop.)
HFSUP - Hair folicle suprabasal keratinocytes (2 pop.)
OB - Outer bulge (1 pop.)
SG - Sebaceous gland (1 pop.)
IMM - Immune cells
MC - Macrophages (2 pop.)
NEUT - Neutrophil (2 pop.)
DC/LC - Dendritic and Langerhans (1 pop.)
TC - Memory T cell (1 pop.)
FIB - Fibroblast-like cells
FIB - Skin fibroblast (3 pop.)
EC - Endothelial cells
EC - Skin endothelial (2 pop.)
NEU - Neuron cells
NEU - Neuron (1 pop.)
VASC - Vascular cells
VSM - Vascular smooth muscle (1 pop.)
IMM
EPI
EC
NEU
FIB
VASC
D Uninfected/Infected visualized on UMAP
E
Suprabasal keratinocyte (spinous + granular)
Epidermis
Basal keratinocyte
Memory T cell
Sebaceous gland
Neutrophil
Hair follicle
Dermis
Macrophage
Bulge
Dendritic/Langerhans
Endothelial
Neuron
VSM
Basal keratinocyte
Dendritic/Langerhans
Endothelial
Fibroblast
Macrophage
Memory T cell
Neuron
Neutrophil
Outer bulge
Sebaceous gland
Suprabasal keratinocyte
Hair follicle
Vasc. smooth muscle
F Top 2 cell type-specific markers in the cell classes
Avg. exprs.
pct. exprs.
H Weighted gene co-expression network analysis
Immune
Neuron
Epithelial
Immune
Epithelial
Endothelial
VSM
Fibroblast
Dendritic/Langerhans
Macrophage
Memory T cell
Neuron
Outer bulge
Basal keratinocyte
Neutrophil
Hair follicle
Suprabasal keratinocyte
Endothelial
Vasc. smooth muscle
Fibroblast
High
Low
G Gene expression correlated with cell classes
Epithelial
Endothelial
Fibroblast
Krt5
Ifi202b
Lgr5
Krt16
Scd1
Pecam1
Fbn1
Immune
Neuron
VSM
Itgax
Mrc1
Arg1
Csf3r
Lck
Gldn
Myh11
High
Low

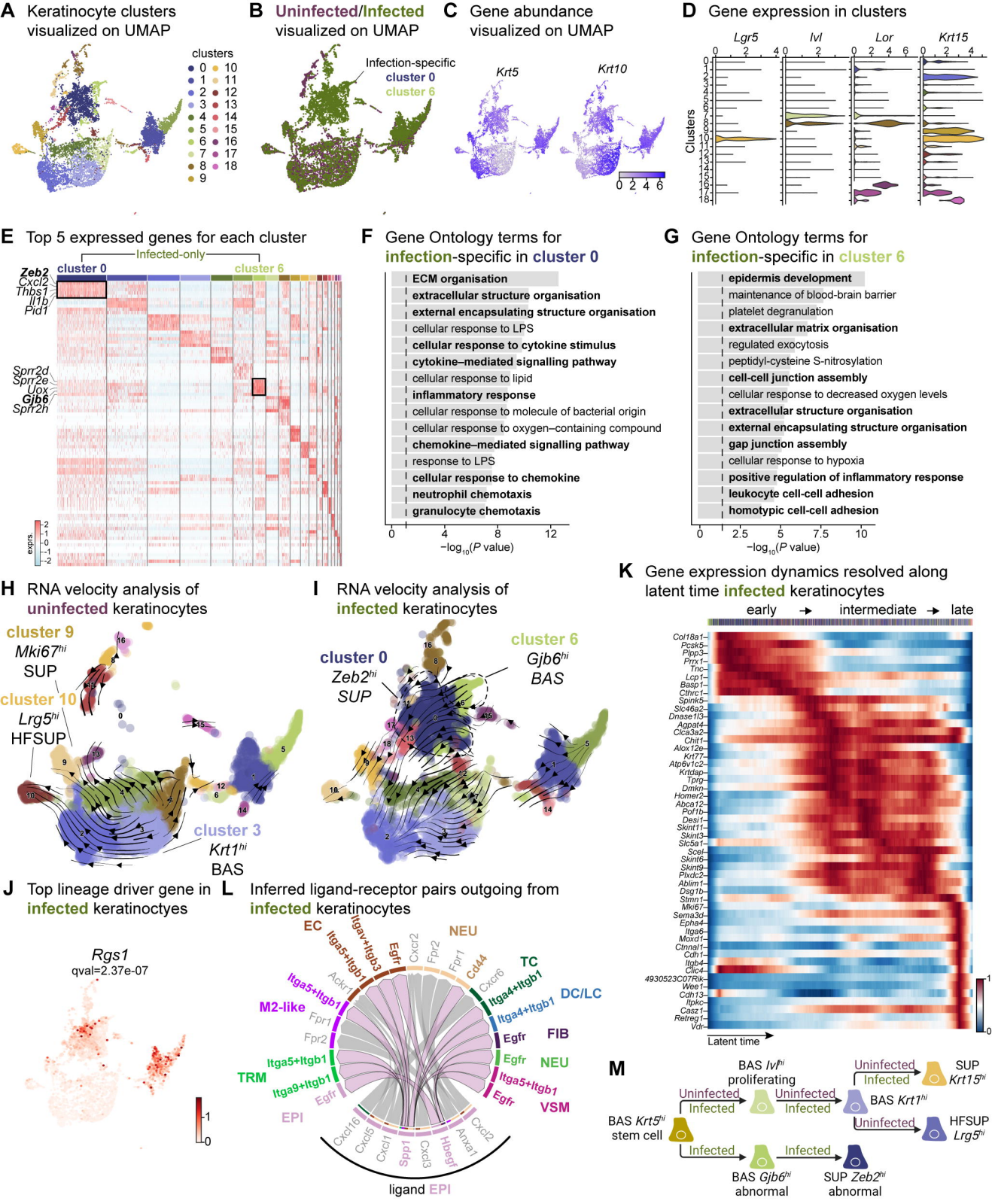
A Keratinocyte clusters visualized on UMAP
clusters
0 1 2 3 4 5 6 7 8 9 10 11 12 13 14 15 16 17 18
B Uninfected/Infected visualized on UMAP
Infection-specific
cluster 0
cluster 6
C Gene abundance visualized on UMAP
Krt5
Krt10
0 2 4 6
D Gene expression in clusters
Lgr5
Ivl
Lor
Krt15
Clusters
E Top 5 expressed genes for each cluster
Infected-only
cluster 0
cluster 6
Zeb2
Cxcl2
Thbs1
Il1b
Pid1
Sprr2d
Sprr2e
Lox
Gjb6
Sprr2h
exprs
F Gene Ontology terms for infection-specific in cluster 0
ECM organisation
extracellular structure organisation
external encapsulating structure organisation
cellular response to LPS
cellular response to cytokine stimulus
cytokine–mediated signalling pathway
cellular response to lipid
inflammatory response
cellular response to molecule of bacterial origin
cellular response to oxygen–containing compound
chemokine–mediated signalling pathway
response to LPS
cellular response to chemokine
neutrophil chemotaxis
granulocyte chemotaxis
−log10(P value)
G Gene Ontology terms for infection-specific in cluster 6
epidermis development
maintenance of blood-brain barrier
platelet degranulation
extracellular matrix organisation
regulated exocytosis
peptidyl-cysteine S-nitrosylation
cell-cell junction assembly
cellular response to decreased oxygen levels
extracellular structure organisation
external encapsulating structure organisation
gap junction assembly
cellular response to hypoxia
positive regulation of inflammatory response
leukocyte cell-cell adhesion
homotypic cell-cell adhesion
−log10(P value)
H RNA velocity analysis of uninfected keratinocytes
cluster 9
Mki67hi
SUP
cluster 10
Lrg5hi
HFSUP
cluster 3
Krt1hi
BAS
I RNA velocity analysis of infected keratinocytes
cluster 0
Zeb2hi
SUP
cluster 6
Gjb6hi
BAS
J Top lineage driver gene in infected keratinoctyes
Rgs1
qval=2.37e-07
K Gene expression dynamics resolved along latent time infected keratinocytes
early
intermediate
late
Latent time
L Inferred ligand-receptor pairs outgoing from infected keratinocytes
EC
Itgav+Itgb3
Itga5+Itgb1
Egfr
Cxcr2
Fpr2
Fpr1
NEU
Cd44
Cxcr6
TC
Itga4+Itgb1
DC/LC
Itga4+Itgb1
FIB
Egfr
NEU
Egfr
Itga5+Itgb1
VSM
Egfr
Cxcl2
Anxa1
Hbegf
Spp1
Cxcl3
Cxcl1
Cxcl5
Cxcl16
EPI
Egfr
Itga9+Itgb1
TRM
Itga5+Itgb1
Itga5+Itgb1
M2-like
Fpr1
Fpr2
Ackr1
ligand EPI
M
BAS Ivlhi proliferating
Uninfected
Infected
Uninfected
Infected
Uninfected
Infected
SUP Krt15hi
BAS Krt1hi
Uninfected
HFSUP Lrg5hi
BAS Krt5hi stem cell
Infected
Infected
BAS Gjb6hi abnormal
SUP Zeb2hi abnormal

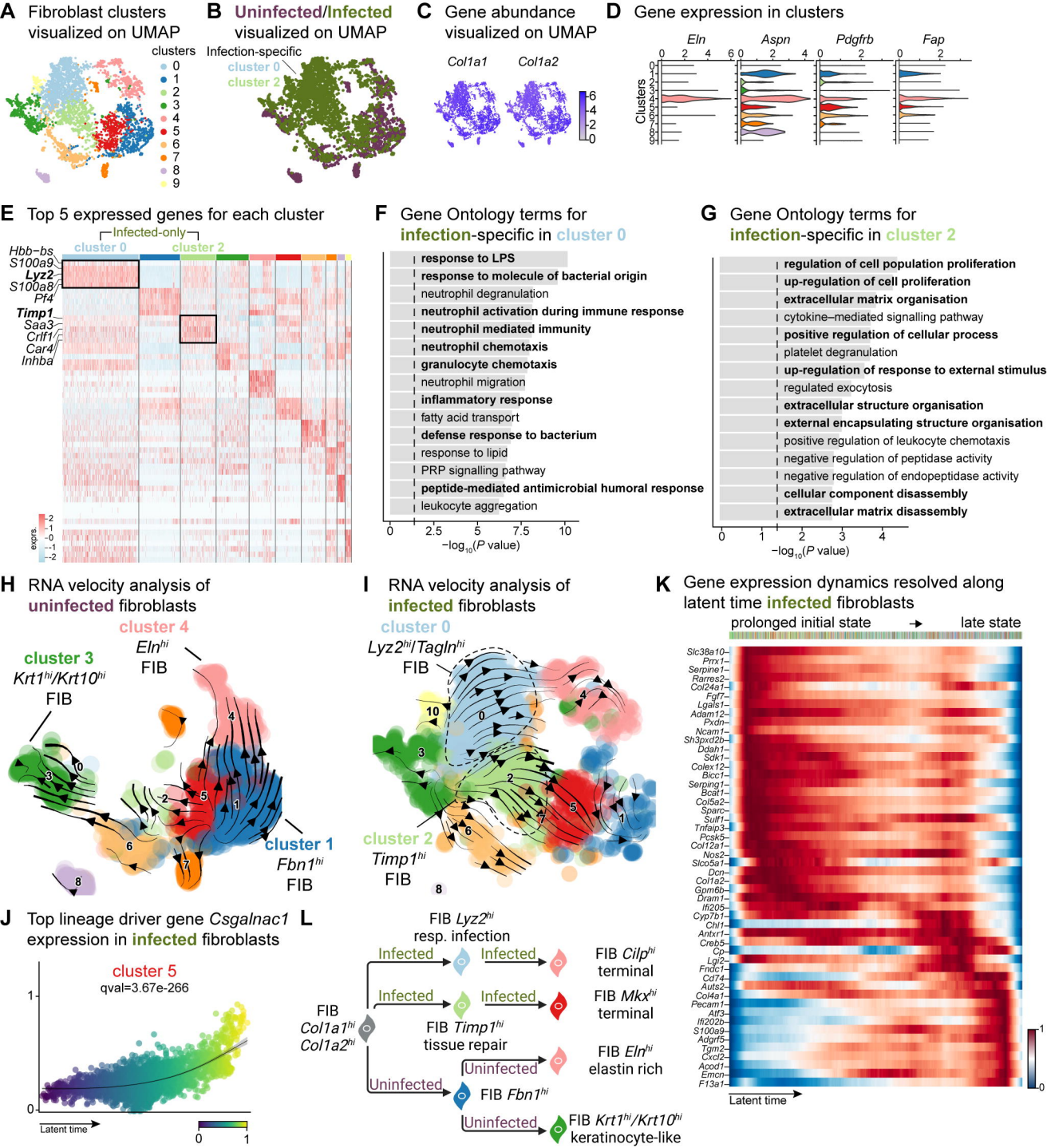
A Fibroblast clusters visualized on UMAP
clusters
0
1
2
3
4
5
6
7
8
9
B Uninfected/Infected visualized on UMAP
Infection-specific
cluster 0
cluster 2
C Gene abundance visualized on UMAP
Col1a1
Col1a2
6
4
2
0
D Gene expression in clusters
Eln
Aspn
Pdgfrb
Fap
Clusters
E Top 5 expressed genes for each cluster
Infected-only
cluster 0
cluster 2
Hbb-bs
S100a9
Lyz2
S100a8
Pf4
Timp1
Saa3
Crlf1
Car4
Inhba
exprs.
F Gene Ontology terms for infection-specific in cluster 0
response to LPS
response to molecule of bacterial origin
neutrophil degranulation
neutrophil activation during immune response
neutrophil mediated immunity
neutrophil chemotaxis
granulocyte chemotaxis
neutrophil migration
inflammatory response
fatty acid transport
defense response to bacterium
response to lipid
PRP signalling pathway
peptide-mediated antimicrobial humoral response
leukocyte aggregation
0
2.5
5
7.5
10
−log10(P value)
G Gene Ontology terms for infection-specific in cluster 2
regulation of cell population proliferation
up-regulation of cell proliferation
extracellular matrix organisation
cytokine–mediated signalling pathway
positive regulation of cellular process
platelet degranulation
up-regulation of response to external stimulus
regulated exocytosis
extracellular structure organisation
external encapsulating structure organisation
positive regulation of leukocyte chemotaxis
negative regulation of peptidase activity
negative regulation of endopeptidase activity
cellular component disassembly
extracellular matrix disassembly
0
1
2
3
4
−log10(P value)
H RNA velocity analysis of uninfected fibroblasts
cluster 4
Eln^hi FIB
cluster 3
Krt1^hi/Krt10^hi FIB
cluster 1
Fbn1^hi FIB
I RNA velocity analysis of infected fibroblasts
cluster 0
Lyz2^hi/Tagln^hi FIB
cluster 2
Timp1^hi FIB
J Top lineage driver gene Csgalnac1 expression in infected fibroblasts
cluster 5
qval=3.67e-266
Latent time
K Gene expression dynamics resolved along latent time infected fibroblasts
prolonged initial state
late state
Slc38a10
Prrx1
Serpine1
Rarres2
Col24a1
Fgf7
Lgals1
Adam12
Pxdn
Ncam1
Sh3pxd2b
Ddah1
Sdk1
Colex12
Bicc1
Serping1
Bcat1
Col5a2
Sparc
Sulf1
Tnfaip3
Pcsk5
Col12a1
Nos2
Slco5a1
Dcn
Col1a2
Gpm6b
Dram1
Ifi205
Cyp7b1
Chi3l
Antxr1
Creb5
Cp
Lgi2
Fndc1
Cd74
Aus2
Col4a1
Pecam1
Atf3
Ifi202b
S100a9
Adgrf5
Tgm2
Cxcl2
Acod1
Emcn
F13a1
Latent time
L
FIB Lyz2^hi resp. infection
Infected
Infected
FIB Cilp^hi terminal
Infected
Infected
FIB Mkx^hi terminal
FIB Col1a1^hi Col1a2^hi
FIB Timp1^hi tissue repair
Uninfected
FIB Eln^hi elastin rich
Uninfected
FIB Fbn1^hi
Uninfected
FIB Krt1^hi/Krt10^hi keratinocyte-like

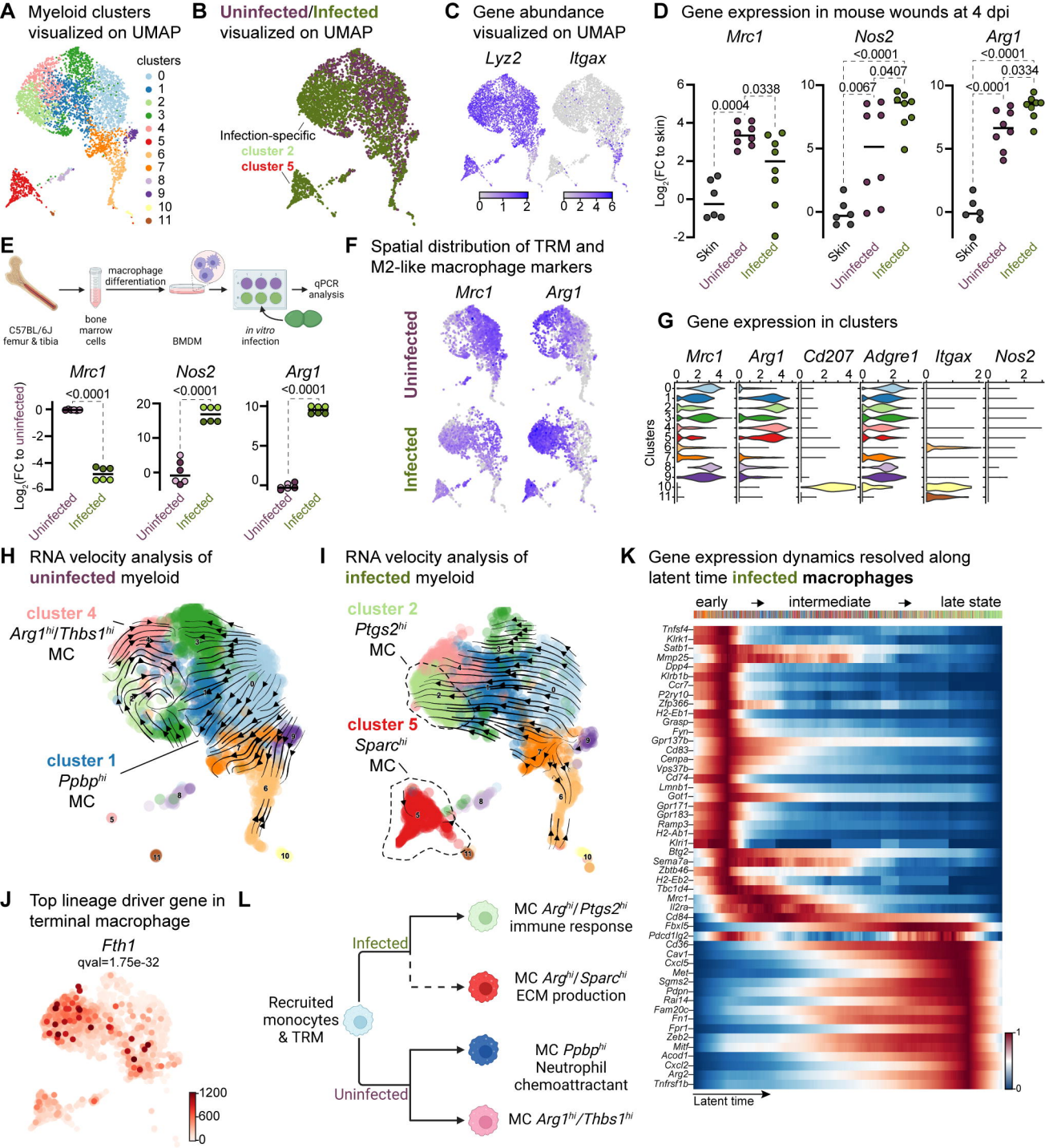
A
Myeloid clusters visualized on UMAP
clusters
0
1
2
3
4
5
6
7
8
9
10
11
B
Uninfected/Infected visualized on UMAP
Infection-specific
cluster 2
cluster 5
C
Gene abundance visualized on UMAP
Lyz2
Itgax
0 1 2
0 2 4 6
D
Gene expression in mouse wounds at 4 dpi
Mrc1
Nos2
Arg1
Log2(FC to skin)
0.0004
0.0338
<0.0001
0.0067
0.0407
<0.0001
<0.0001
0.0334
Skin
Uninfected
Infected
E
C57BL/6J femur & tibia
bone marrow cells
macrophage differentiation
BMDM
in vitro infection
qPCR analysis
Mrc1
Nos2
Arg1
<0.0001
<0.0001
<0.0001
Log2(FC to uninfected)
Uninfected
Infected
F
Spatial distribution of TRM and M2-like macrophage markers
Mrc1
Arg1
Uninfected
Infected
G
Gene expression in clusters
Mrc1
Arg1
Cd207
Adgre1
Itgax
Nos2
Clusters
H
RNA velocity analysis of uninfected myeloid
cluster 4
Arg1hi/Thbs1hi
MC
cluster 1
Ppbphi
MC
I
RNA velocity analysis of infected myeloid
cluster 2
Ptgs2hi
MC
cluster 5
Sparchi
MC
J
Top lineage driver gene in terminal macrophage
Fth1
qval=1.75e-32
1200
600
0
K
Gene expression dynamics resolved along latent time infected macrophages
early
intermediate
late state
Tnfsf4
Klrk1
Satb1
Mmp25
Dpp4
Klrb1b
Ccr7
P2ry10
Zfp366
H2-Eb1
Grasp
Fyn
Gpr137b
Cd83
Cenpa
Vps37b
Cd74
Lmnb1
Golt1
Gpr171
Gpr183
Ramp3
H2-Ab1
Klri1
Btg2
Sema7a
Zbtb46
H2-Eb2
Tbc1d4
Mrc1
Il2ra
Cd84
Fbxl5
Pdcd1lg2
Cd36
Cav1
Cxcl5
Met
Sgms2
Pdpn
Ral14
Fam20c
Fn1
Fpr1
Zeb2
Mitf
Acod1
Cxcl2
Arg2
Tnfrsf1b
Latent time
1
0
L
Recruited monocytes & TRM
Infected
Uninfected
MC Arghi/Ptgs2hi
immune response
MC Arghi/Sparchi
ECM production
MC Ppbphi
Neutrophil chemoattractant
MC Arg1hi/Thbs1hi

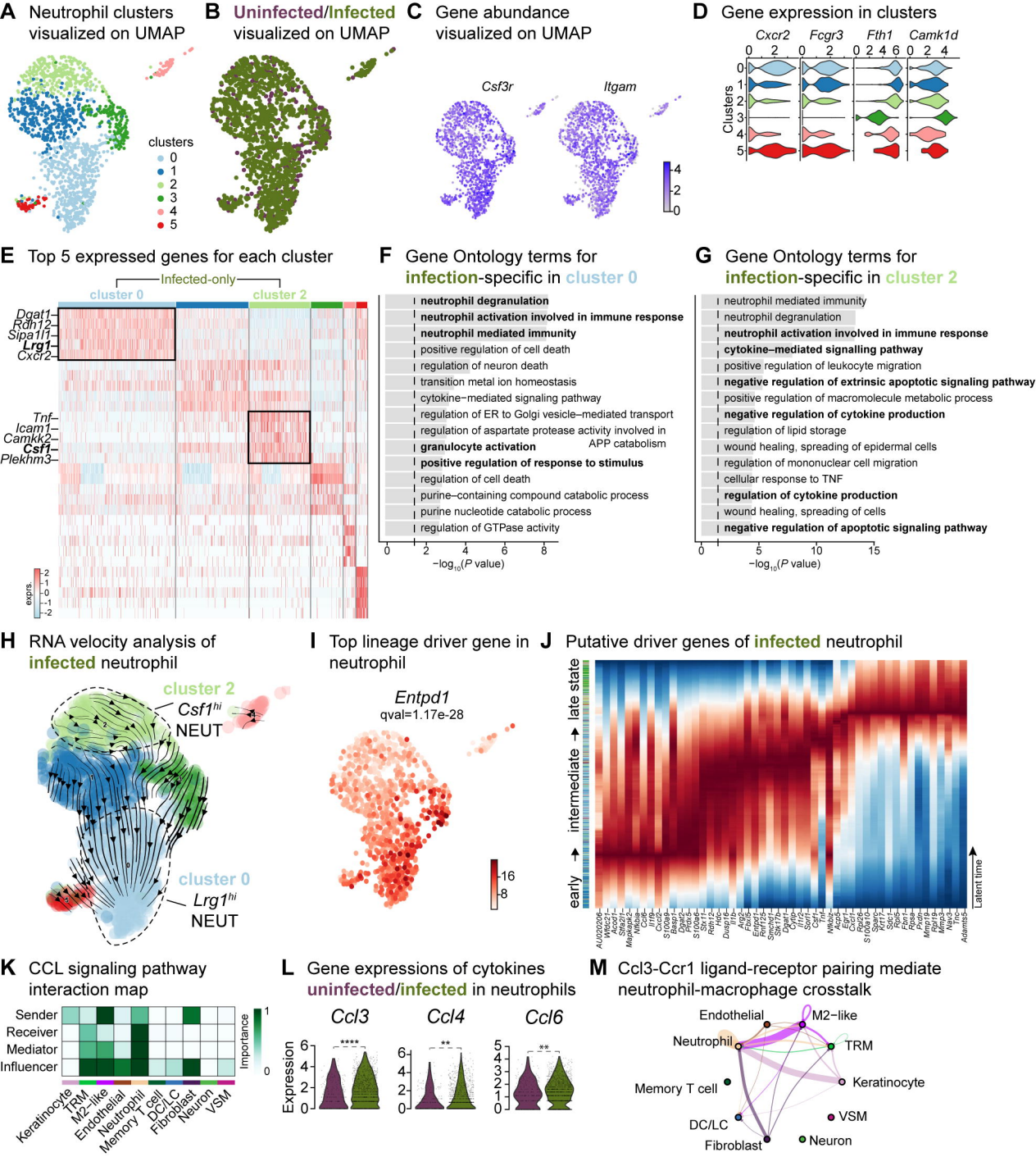
A Neutrophil clusters visualized on UMAP
clusters
0
1
2
3
4
5
B Uninfected/Infected visualized on UMAP
C Gene abundance visualized on UMAP
Csf3r
Itgam
4
2
0
D Gene expression in clusters
Cxcr2
Fcgr3
Fth1
Camk1d
Clusters
E Top 5 expressed genes for each cluster
Infected-only
cluster 0
cluster 2
Dgat1
Rdh12
Sipa1l1
Lrg1
Cxcr2
Tnf
Icam1
Camkk2
Csf1
Plekhm3
exprs.
F Gene Ontology terms for infection-specific in cluster 0
neutrophil degranulation
neutrophil activation involved in immune response
neutrophil mediated immunity
positive regulation of cell death
regulation of neuron death
transition metal ion homeostasis
cytokine−mediated signaling pathway
regulation of ER to Golgi vesicle−mediated transport
regulation of aspartate protease activity involved in APP catabolism
granulocyte activation
positive regulation of response to stimulus
regulation of cell death
purine−containing compound catabolic process
purine nucleotide catabolic process
regulation of GTPase activity
−log10(P value)
G Gene Ontology terms for infection-specific in cluster 2
neutrophil mediated immunity
neutrophil degranulation
neutrophil activation involved in immune response
cytokine−mediated signalling pathway
positive regulation of leukocyte migration
negative regulation of extrinsic apoptotic signaling pathway
positive regulation of macromolecule metabolic process
negative regulation of cytokine production
regulation of lipid storage
wound healing, spreading of epidermal cells
regulation of mononuclear cell migration
cellular response to TNF
regulation of cytokine production
wound healing, spreading of cells
negative regulation of apoptotic signaling pathway
−log10(P value)
H RNA velocity analysis of infected neutrophil
cluster 2
Csf1hi
NEUT
cluster 0
Lrg1hi
NEUT
I Top lineage driver gene in neutrophil
Entpd1
qval=1.17e-28
16
8
J Putative driver genes of infected neutrophil
late state
intermediate
early
Latent time
K CCL signaling pathway interaction map
Sender
Receiver
Mediator
Influencer
Importance
Keratinocyte
TRM
M2−like
Endothelial
Neutrophil
Memory T cell
DC/LC
Fibroblast
Neuron
VSM
L Gene expressions of cytokines uninfected/infected in neutrophils
Ccl3
Ccl4
Ccl6
Expression
M Ccl3-Ccr1 ligand-receptor pairing mediate neutrophil-macrophage crosstalk
Endothelial
M2−like
Neutrophil
TRM
Keratinocyte
Memory T cell
VSM
DC/LC
Fibroblast
Neuron

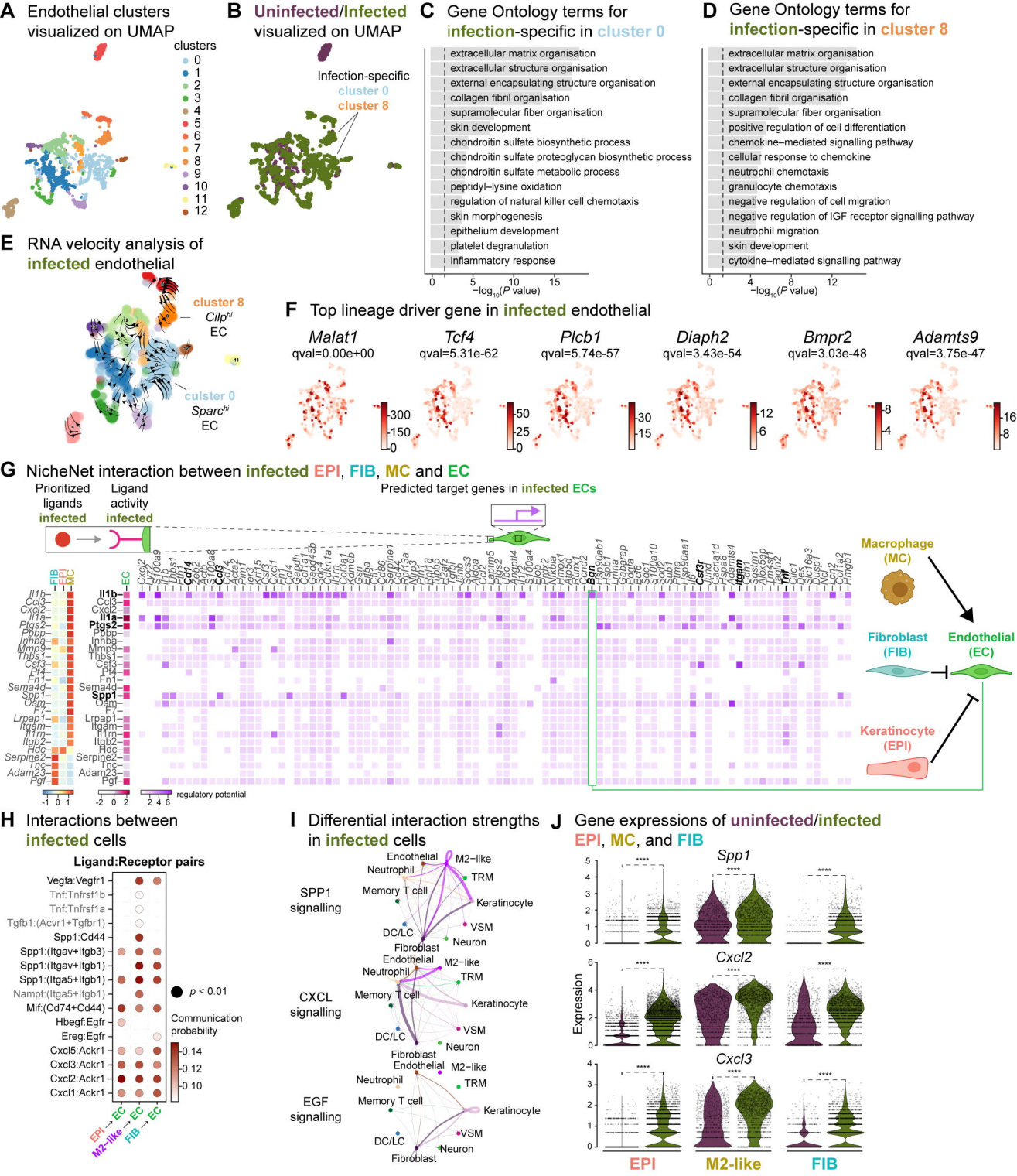
A Endothelial clusters visualized on UMAP
clusters
0
1
2
3
4
5
6
7
8
9
10
11
12
B Uninfected/Infected visualized on UMAP
Infection-specific
cluster 0
cluster 8
C Gene Ontology terms for infection-specific in cluster 0
extracellular matrix organisation
extracellular structure organisation
external encapsulating structure organisation
collagen fibril organisation
supramolecular fiber organisation
skin development
chondroitin sulfate biosynthetic process
chondroitin sulfate proteoglycan biosynthetic process
chondroitin sulfate metabolic process
peptidyl–lysine oxidation
regulation of natural killer cell chemotaxis
skin morphogenesis
epithelium development
platelet degranulation
inflammatory response
0
5
10
15
−log10(P value)
D Gene Ontology terms for infection-specific in cluster 8
extracellular matrix organisation
extracellular structure organisation
external encapsulating structure organisation
collagen fibril organisation
supramolecular fiber organisation
positive regulation of cell differentiation
chemokine–mediated signalling pathway
cellular response to chemokine
neutrophil chemotaxis
granulocyte chemotaxis
negative regulation of cell migration
negative regulation of IGF receptor signalling pathway
neutrophil migration
skin development
cytokine–mediated signalling pathway
0
4
8
12
−log10(P value)
E RNA velocity analysis of infected endothelial
cluster 8
Cilphi
EC
culster 0
Sparchi
EC
F Top lineage driver gene in infected endothelial
Malat1
qval=0.00e+00
Tcf4
qval=5.31e-62
Plcb1
qval=5.74e-57
Diaph2
qval=3.43e-54
Bmpr2
qval=3.03e-48
Adamts9
qval=3.75e-47
G NicheNet interaction between infected EPI, FIB, MC and EC
Prioritized ligands
Ligand activity
infected
Predicted target genes in infected ECs
EPI
FIB
MC
EC
Il1b
Ccl3
Cxcl2
Il1a
Ptgs2
Pbpn
Inhba
Mmp9
Thbs1
Csf3
Pf4
Fn1
Sema4d
Spp1
Osm
F7
Lrpap1
Itgam
Il1rn
Itgb2
Hdc
Serpine2
Tnc
Adam23
Pgf
Cd14
Ccl3
Ccl4
Ccl5
Cxcl1
Cxcl2
Cxcl3
Cxcr4
Cd14
Gapdh
Gadd45b
Sdc4
Cdkn1a
Acta2
Plin1
Ier3
Ccl5
Csf3
Cd14
Cxcl1
Cxcl2
Cxcl3
Cxcr4
Cd14
Cd86
Serpine1
Rnf13a
Dhx3
Sp110
Tubb5
Tcf4
Junb
Ifitm3
Socs3
Ccl2
Laptm5
Ccl2
Dbi
Angptl4
Il10ra4
Eiob
Phlda2
Hmox1
Atp5d
Cox7c
Cox7a2
Bgn
Hsp90ab1
Hsp1
Cabrap
Gapdh
Sdc1
S100a10
Sod1
Pim1
Hsp90aa1
Hsp1
Csf3r
Jund
Cacna1d
Cxcr4
Adamts4
Itgam
Gm
Sostdc1
Slc7a11
Ajox3ap
Tmem37
Tnf
Ccl2
Ccl1
Slc16a3
Dusp1
Ncf2
Col1a2
Hmgb1
regulatory potential
-1 0 1
-2 0 2
2 4 6
Macrophage (MC)
Fibroblast (FIB)
Endothelial (EC)
Keratinocyte (EPI)
H Interactions between infected cells
Ligand:Receptor pairs
Vegfa:Vegfr1
Tnf:Tnfrsf1b
Tnf:Tnfrsf1a
Tgfb1:(Acvr1+Tgfbr1)
Spp1:Cd44
Spp1:(Itgav+Itgb3)
Spp1:(Itgav+Itgb1)
Spp1:(Itga5+Itgb1)
Nampt:(Itga5+Itgb1)
Mif:(Cd74+Cd44)
Hbegf:Egfr
Ereg:Egfr
Cxcl5:Ackr1
Cxcl3:Ackr1
Cxcl2:Ackr1
Cxcl1:Ackr1
p < 0.01
Communication probability
0.14
0.12
0.10
EPI → EC
M2-like → EC
FIB → EC
I Differential interaction strengths in infected cells
SPP1 signalling
CXCL signalling
EGF signalling
Endothelial
Neutrophil
M2−like
TRM
Memory T cell
Keratinocyte
VSM
DC/LC
Neuron
Fibroblast
J Gene expressions of uninfected/infected EPI, MC, and FIB
Spp1
Cxcl2
Cxcl3
Expression
****
EPI
M2-like
FIB